



52 in various form. E.g., Pellicciotti et al. (2005) included potential solar radiation and parameterized albedo of the
53 snow surface into the modelling, allowing for sub-daily time steps of the calculations.

54 The most sophisticated type of snow models solves the energy balance of the snow surface, requiring a more or
55 less complex description of the short- and longwave radiative fluxes, the turbulent fluxes of sensible and latent
56 heat, the advective heat flux supplied by solid or liquid precipitation and the soil heat flux at the lower boundary
57 of the snow pack. To solve the energy balance equation, these models divide the snowpack into several layers and
58 iteratively compute the state variables for each single layer, usually including respective snow height, density,
59 liquid water content and temperature (e.g., Vionnet et al., 2012; Lehning et al., 1999; Essery, 2015). Sophisticated
60 model concepts of this type also include methods for the correction of the effect of atmospheric stability on the
61 turbulent fluxes (e.g., Sauter et al., 2020).

62 For distributed snow model applications in complex mountain terrain, shadowing of the solar radiation beam and
63 – depending on the application and the considered scale – lateral snow redistribution processes like blowing snow
64 or snow slides should be considered in the modeling, especially if simulations are conducted for longer time
65 horizons (e.g., Vionnet et al., 2021; Quéno et al., 2023). Distributed model applications also require sophisticated
66 methods for the spatial interpolation of the local meteorological station recordings (see, e.g., MeteolO; Bavay and
67 Egger, 2014), or downscaling procedures to utilize gridded weather or climate model output to force the
68 simulations.

69 Very recently, methods of artificial intelligence have undergone a hype-like push for development of new
70 modelling approaches: these make use of the forcing variables governing any processes changing a system, and
71 time series of observations of its state. In a certain perspective these models are similar to calibrated models, with
72 empiricism thereby replaced by statistics. However, the same limitations exist for such statistical approaches like
73 for the empirical ones in terms of transferability of their application in space and time. First attempts also exist to
74 complement complex physical snow models with data-driven machine learning approaches, e.g. the “Deep
75 Learning national scale 1 km resolution snow water equivalent (SWE) prediction model“
76 (<https://github.com/whitelighting450/SWEML>; last access: March 7, 2024). Similar developments are
77 undertaken in the field of weather forecasting (e.g., Lam et al., 2023), with respective implications on the
78 predictability of the snow cover evolution. It can be expected that in this domain many innovations will emerge in
79 the near future.

80 Most of the sophisticated energy balance snow (hydrological) models which are currently in development are
81 available as open source projects for the public, such as Surfex (<https://www.umr-cnrm.fr/surfex>; last access:
82 March 7, 2024), CRHM (<https://github.com/CentreForHydrology/CRHM>; last access: March 7, 2024), FSM
83 (<https://github.com/RichardEssery/FSM>; last access: March 7, 2024), SNOWPACK (<https://snowpack.slf.ch>; last
84 access: March 7, 2024), COSIPY (<https://github.com/cryotools/cosipy>; last access: March 7, 2024), or, as
85 described in the following, openAMUNDSEN (Hanzer et al., 2023).

86 openAMUNDSEN v 0.9, the snow-hydrological model described herein, compromises many of the presented
87 snow model principles, from simple empirical approaches to coupled energy and mass balance calculations. The
88 model mainly is built upon a comprehensive, physically based description of snow processes typical for high
89 mountain regions. In particular, the main features of the model include:

- 90 • Spatial interpolation of scattered meteorological point measurements using a combined lapse rate/inverse
91 distance weighting scheme
- 92 • Calculation of solar radiation taking into account terrain slope and orientation, hillshading and atmospheric
93 transmission losses as well as gains due to scattering, absorption, and multiple reflections between the snow
94 surface and clouds
- 95 • Adjustment of precipitation using several correction functions for wind-induced undercatch and lateral
96 redistribution of snow using terrain-based parameterizations
- 97 • Simulation of the snow and ice mass and energy balance using either a multi-layer scheme or a bulk scheme
98 using four separate layers for new snow, old snow, firm and ice
- 99 • Alternatively, a temperature index/enhanced temperature index method, the latter considering potential solar
100 radiation and albedo of the surface
- 101 • Usage of arbitrary timesteps (e.g. 10 minutes, hourly, daily) while resampling of forcing data to the desired
102 temporal resolution if necessary
- 103 • Flexible output of time series including arbitrary model variables for selected point locations in NetCDF or
104 CSV format



- 105 • Flexible output of gridded model variables, either for specific dates or periodically (e.g., daily or monthly),
106 optionally aggregated to averages or totals in NetCDF, GeoTIFF or ASCII grid format
107 • Built-in generation of future meteorological data time series as model forcing with a given trend using a
108 bootstrapping algorithm for the available historical time series of the meteorological recordings
109 • Live view window for illustrating selectable variables of the model state during runtime.

110 Together with the model, a comprehensive set of data that can be used to run the model for the upper Rofental
111 (Tyrol/Austria, 98.1 km²) is available at Pangaea (Strasser et al., 2018; Warscher et al., 2024) as well as in form
112 of an openAMUNDSEN example setup on GitHub (<https://github.com/openamundsen/openamundsen-examples>;
113 last access: March 7, 2024). This data can freely be used to setup and run the model for this catchment and to
114 conduct a multitude of simulation experiments like sensitivity tests and evaluation. This data can also serve as
115 example to be replaced by data from other catchments or sites. The Rofental is used in the following as example
116 site to illustrate the functionalities of the model.

117 2 Model evolution

118 The AMUNDSEN model has a development history of well over twenty years. Originally, the model was prepared
119 to compute fields of meteorological variables, snow albedo and melt with a new enhanced temperature index
120 approach (Pellicciotti et al., 2005). Later, a simple surface energy balance method based on ESCIMO¹ (Strasser
121 and Mauser, 2001) was integrated. The model was then applied and continuously improved to simulate snow
122 hydrological variables for Haut Glacier d’Arolla (Strasser et al., 2004) and the high alpine region of the
123 Berchtesgaden National Park (Strasser, 2008). Strasser et al. (2008) investigated the sublimation losses of the
124 alpine snow cover from the ground and vegetated surfaces, as well as during blowing snow events. In Strasser et
125 al. (2011), snow-canopy processes were modelled for a chess-board pattern of various forest stands and open areas
126 on an idealized mountain. The simple bulk energy balance core of the model also exists as a spread-sheet based
127 point scale scheme where only hourly meteorological variables have to be pasted in to run the snow simulations
128 for a particular observation site (Strasser and Marke, 2010). This spread-sheet based model was later extended by
129 the snow-canopy interaction processes that were already implemented in AMUNDSEN (Marke et al., 2016). The
130 energy balance approach was continuously further developed, e.g. with an iterative procedure to account for
131 atmospheric stability (after Weber, 2008) or with the introduction of a 4-layer scheme (new snow, old snow, firm,
132 glacier ice; Hanzer et al., 2016). Hanzer et al. (2014) developed a module for the production of technical snow on
133 skiing slopes. Historical and future snow conditions for Austria were determined with the model by Marke et al.
134 (2015) and Marke et al. (2018), respectively. Hanzer et al. (2016) presented a parameterization for lateral snow
135 redistribution based on topographic openness, and multi-level spatiotemporal validation as a systematic,
136 independent, complete and redundant validation procedure. The hydrological response and glacier evolution in a
137 changing climate was investigated by Hanzer et al. (2018) for the Ötztal Alps in Austria. Modelled SWE also
138 provided a reference for the fusion with satellite-data derived snow distribution maps in a machine learning
139 framework (De Gregorio et al., 2019a and b, respectively), or to determine distributed glacier mass balance
140 (Podsiadlo et al., 2020). Pfeiffer et al. (2021) used the model to determine the amount of liquid water provided for
141 infiltration by snowmelt and rainfall for determining conditions that fostered the motion of a landslide in the
142 Tyrolean Alps. With the transition to the open source project openAMUNDSEN, the multi-layer approach by
143 Essery (2015) was integrated into the model as further alternative to compute the mass and energy balance of a
144 layered snow pack. Finally the openAMUNDSEN model has been used to simulate the entire process of snow
145 management and snow conditions for the slopes in skiing areas (Hanzer et al., 2020, Ebner et al., 2021).

146 The first distributed version of the AMUNDSEN model was developed in IDL (= Interactive Data Language, see
147 <https://www.nv5geospatialsoftware.com/Products/IDL>; last access: March 7, 2024), originally documented in
148 Strasser (2008) and – in a more recent evolutionary stage – in Hanzer et al. (2018). Recently, the model code was
149 completely re-programmed in Python and transferred into an open source project (Hanzer et al. 2023); this was
150 the moment when the model was renamed to “openAMUNDSEN”. An online documentation is currently in
151 production (<https://doc.openamundsen.org>; last access: March 7, 2024). New developments which are not yet
152 available online in the GitHub repository will be published there after comprehensive testing.

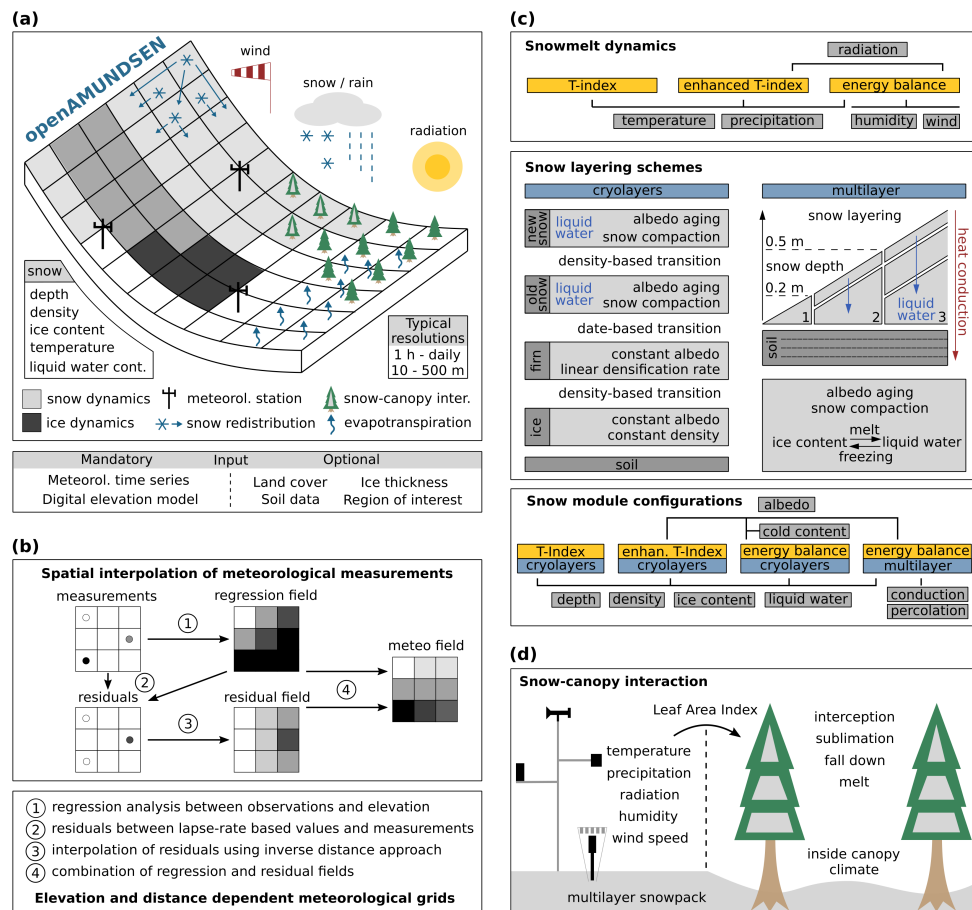
¹ The first point-scale version of the snow model was named Energy balance Snow Cover Integrated MOdel (ESCIMO) and programmed in Fortran (Strasser and Mauser, 2001). Later, when the first distributed version was developed in IDL it was renamed to AMUNDSEN.



153 3 Model concept

154 3.1 General structural design

155 The fundamental principles and most important capabilities of the model are shown in the general overview (figure
 156 1a). The region for which openAMUNDSEN is to be set up is a rectangle comprised by a digital elevation model
 157 (DEM) in raster format. This DEM defines the extent and resolution for which the model computations are
 158 performed. The model is capable to simulate the mass balance of both snow and/or glacier ice surfaces, as well as
 159 lateral redistribution of snow, snow-canopy interaction and evapotranspiration from different land cover types.
 160 Irregular observations of meteorological stations or gridded output from any kind of raster model are distributed
 161 over the domain by means of a combined inverse distance procedure considering an elevation gradient and spatially
 162 interpolated residuals of the recordings (figure 1b). Several approaches of varying complexity are available to
 163 compute surface melt, from a simple temperature-index method over an enhanced index approach considering
 164 temperature, potential solar radiation and albedo to sophisticated energy balance methods (figure 1c). These melt
 165 approaches can be combined with different layering schemes in a total of four different snow model configurations.
 166 Each of these configurations can be applied to forest conditions, where a modified set of the meteorological
 167 variables is provided to account for the effect of the trees on the inside-canopy microclimate, parameterized by
 168 means of the Leaf Area Index as the variable describing the characteristics of the forest (figure 1d).

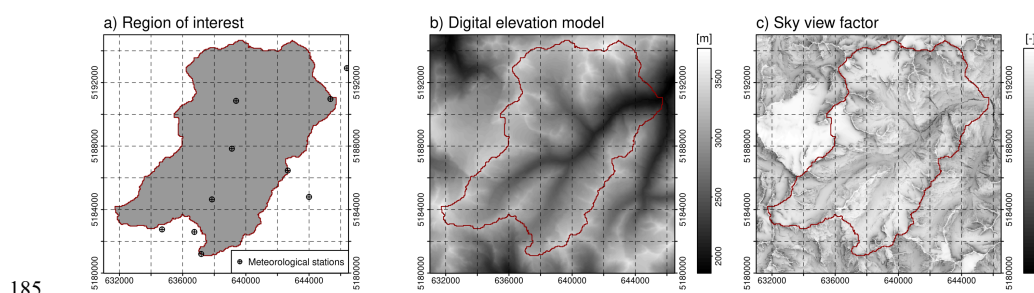


169

170 Figure 1: Schematic representation of a domain modelled with the snow-hydrological model openAMUNDSEN
 171 (a), spatial interpolation of the meteorological measurements (b), snowmelt dynamics and snow layering schemes
 172 (c) and scaling of observed to inside-canopy meteorological conditions for the simulation of snow-canopy
 173 interaction processes (d) in the model.



174 To save computational time, it is possible to define an irregular region of interest (ROI; i.e., a sub-quantity of
 175 pixels); outside this area only some required calculations for the interpolation of the meteorological variables will
 176 be computed (figure 2a). Typically, a ROI is a watershed area for which water balance components are aggregated
 177 from the single pixel values, and resulting streamflow volume can be compared to gauge recordings (Hanzer et
 178 al., 2018). Weather stations to be considered can also be located outside the ROI, and even outside the DEM area;
 179 however, in the latter case they cannot be considered for the determination of shadow areas or regional-scale
 180 albedo which is used to estimate the diffuse radiative fluxes by multiple scattering between the surface and the
 181 atmosphere. Extent and resolution of the DEM defines the cell size and the geometry of all other raster layers
 182 produced in the simulations (figure 2b). From this DEM, several derived variables such as slope, aspect and sky
 183 view factor are calculated (figure 2c). The sky view factor is the portion of the visible sky, i.e. the ratio of visible
 184 sky that can be seen from a pixel location to the entire hemisphere that contains both visible and obstructed sky.



185

186 Figure 2: Region of interest of the openAMUNDSSEN example application to the Rofental (Tyrolean Alps/Austria)
 187 with location of weather stations in- and outside the region of interest (a), digital elevation model (b) and sky
 188 view factor (c). The red line is the watershed divide of the Rofental for the gauge at Vent (1891 m a.s.l.).

189 The meteorological forcing for the simulations typically consists of time series of temperature, relative humidity,
 190 precipitation, global radiation and wind speed. To accurately track the daily course of radiative energy – usually
 191 the most important component of the energy for melt – the time step in the modelling in most applications is
 192 hourly. It is also possible to use sub-hourly time steps, or, to save computational time, the model computations can
 193 also be limited to 2- or 3-hourly time steps, if the optional temperature index approach is selected the time step
 194 also can be set to daily. For the case that specific submodules are activated for a model run (e.g., snow-canopy
 195 interaction, evapotranspiration), various other spatial input fields have to be prescribed (e.g., land cover, soil,
 196 catchment boundaries).

197 When using meteorological station data as input the minimum number of stations required is one. This station
 198 should provide a continuous series of measurements without gaps. If more than one weather station exists, missing
 199 values at a particular site are replaced by the respective results from the interpolation procedure. Where recordings
 200 exist, the interpolated values might slightly differ due to the difference in altitude between the exact location of
 201 the station and the grid pixel in which it is located (and for which the meteorological field is interpolated).
 202 Alternatively to station recordings, it is also possible to provide already gridded meteorological fields as input to
 203 the model, e.g. output data from numerical weather prediction or climate models.

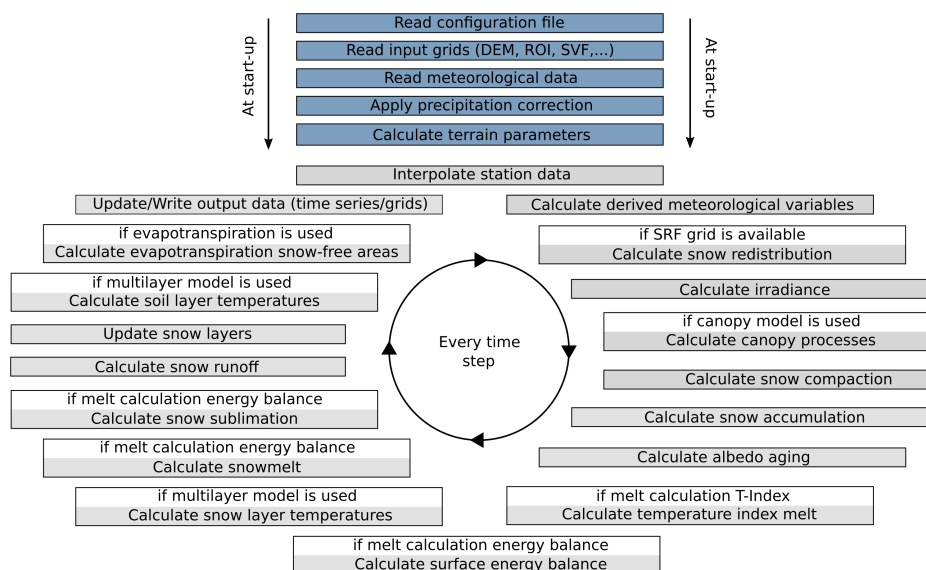
204 The model simulations are performed for each pixel and each timestep (figure 3). Prior to these pixel-wise
 205 computations for the raster domain a set of general computations for the model run are performed: after reading
 206 the input data the terrain parameters are computed from the DEM, and precipitation correction parameters are
 207 computed (as described in 3.5). Then the time-dependent computations for all pixels of the domain start, in a loop
 208 from the first to the last time step of the particular simulation run. Several modules are subject to options which
 209 can be set in a configuration file in text format.

210 The results of the computations can be written to file either as time series for an arbitrary number of pixels (in
 211 NetCDF or CSV format), or as gridded model variables for specific selected dates or periodically (e.g., daily,
 212 monthly, yearly), optionally aggregated to averages or totals. Possible formats include NetCDF, GeoTIFF or
 213 ASCII grid.

214 To keep spin-up modelling times to an acceptable minimum, state variables can be imported as raster grids to
 215 initialize an openAMUNDSSEN model run. Some state variables can also be computed prior to the model run. E.g.,
 216 if glacier outlines are available, the initial ice thickness distribution can be calculated using the approach by Huss



217 and Farinotti (2012). Volumetric balance fluxes of individual glaciers can be calculated from mass balance
 218 gradients and constants. Surface elevations and glacier outlines are usually published in glacier inventories
 219 (<https://wgms.ch>; last access: January 1, 2024), e.g. for Austria in Fischer et al. (2015).



220

221 Figure 3: Flowchart showing the repetitive circle of a typical openAMUNDSEN calculation. The reading of the
 222 input is succeeded by the computation of several precipitation correction and terrain parameters. After that, the
 223 loop for all time steps of the model run is entered.

224 3.2 Temporal and spatial discretization

225 Usually the model is driven with a temporal resolution according to the one of the used meteorological forcing
 226 variables. For model applications which require a higher temporal resolution (or if only daily recordings are
 227 available) methods exist to disaggregate the measurements accordingly (e.g. MELODIST, Förster et al., 2016).
 228 Any aggregation is done during runtime. Output temporal resolution can hence also be any aggregate of the original
 229 computation resolution – usually daily, monthly and yearly. All this is arbitrarily set in the model configuration
 230 prior to the model run. The minimum spatial resolution is not limited. Theoretically, a 1 m or even higher resolution
 231 (e.g., laser-scan derived) DEM can be used as basis for the model simulation. A comparatively high resolution
 232 thereby is beneficial for adequately capturing all small-scale processes shaping the snow cover distribution in
 233 complex terrain. However, it is questionable if such computational effort is meaningful with respect to the
 234 availability and quality of the forcing data and to the scale of the considered processes. According to our
 235 experiences from typical mountain catchments in the European Alps a resolution between 10 m and 1000 m is
 236 often a good compromise between detail representation and computational efficiency. The size of the modelled
 237 domains can be anything between one pixel and several tens of thousand square kilometers (see figure 1a). De
 238 Gregorio et al. (2019a, b), e.g., successfully applied the model for the Euregio Tyrol/South Tyrol/Trentino with
 239 26254 km².

240 3.3 Spatial interpolation of meteorological measurements

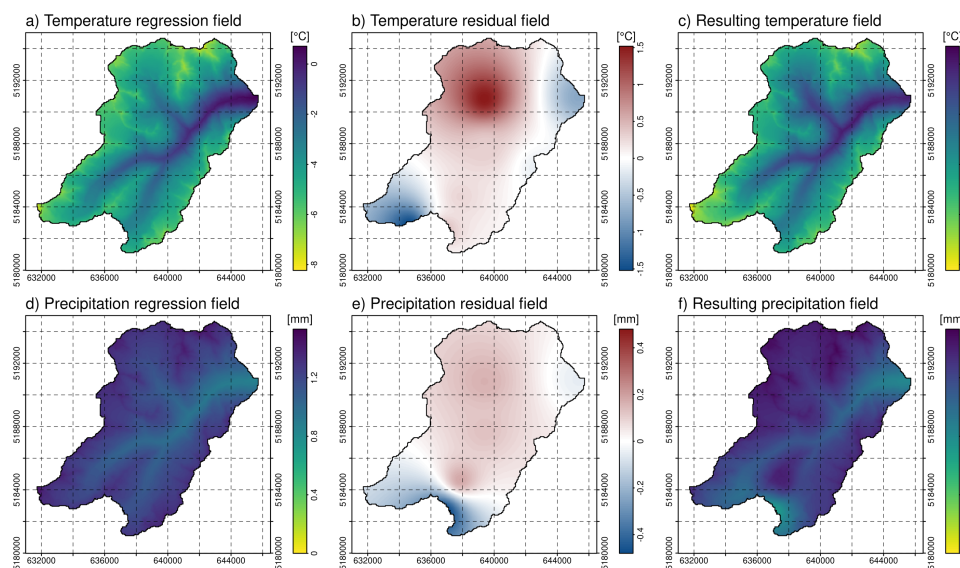
241 openAMUNDSEN includes a meteorological preprocessor for the spatial interpolation of scattered point
 242 measurements, irrespective whether these are provided irregularly (weather station recordings) or arranged as a
 243 regular grid (weather or climate model output). In the latter case, the meteorological variables are resampled to
 244 grids with the given DEM spatial resolution. The minimum forcing required by the model are recordings of
 245 temperature and precipitation (when running in temperature index mode). For energy balance calculations, relative
 246 humidity, global radiation (or cloudiness) and wind speed are required as well. If meteorological time series from
 247 station recordings are used as input, the model interpolates the measurements from their geographical locations to
 248 each cell of the ROI (figure 4). In most simulation cases, only recordings of the meteorological variables for the 2



249 m observation level are available (the distance between a variable snow surface and the sensor height can be
250 corrected for in the modelling). For each model time step,

- 251 • a regression analysis between observations and the associated station elevation is performed to derive an
252 elevation-dependent trend function
- 253 • the derived function is applied to all cells of the DEM to create a trend field for each meteorological variable,
254 the “regression field” (4a and d)
- 255 • the residuals for all station locations are calculated by subtracting the calculated regression value for the
256 station elevation from the actual measurement at the station location for the current time step,
- 257 • the residuals from the station locations (raster cells) are interpolated to the grid using an inverse distance
258 weighting (IDW) method, the “residual field” (4b and e),
- 259 • the interpolated residual field is added to the regression field, which results in elevation- and distance-
260 dependent interpolated fields for all meteorological variables (4 c and f).

261 Figure 4 exemplarily shows the steps of this IDW-based interpolation procedure for temperature and precipitation,
262 respectively. It can be seen that for both temperature and precipitation a dependency of the recordings with
263 elevation does exist (figure 4a and d), but locally some deviations of the measurements from the trend occur (figure
264 4b and e). In the result both patterns are considered. This procedure automatically fills potential gaps in the
265 observation time series at the weather station locations.



266

267 Figure 4: Regression trend field, IDW residual field and the resulting meteorological field, i.e. sum of the two for
268 the spatial interpolation of meteorological variables in each single time step, exemplarily shown for temperature
269 (a, b and c) and for precipitation (d, e and f) on 24/12/2019 at 10 am in the Rofental.

270 Instead of the dynamic lapse rates calculated from the point data in each time step, prescribed average monthly
271 gradients can be used as well, e.g. following Liston and Elder (2006).

272 Precipitation phase is determined by either air temperature or wet-bulb temperature thresholds (wet-bulb
273 temperature is computed by iteratively solving the psychrometric equation). For both methods, a temperature
274 transition range is defined. Above this transition range, precipitation is determined as liquid, and as solid below
275 the lower end of the temperature range, respectively. Within the defined temperature range, the fractions of
276 solid/liquid precipitation are linearly distributed between 100 % liquid at the upper and 100 % solid at the lower
277 end of the range with 50 % liquid/solid fraction of precipitation at the threshold temperature.



278 3.4 Radiative fluxes

279 Incoming global radiation strongly varies in time and space depending on terrain characteristics, position of the
 280 sun and atmospheric conditions. Hence, openAMUNDSEN calculates potential global radiation for each grid cell
 281 based on local aspect and slope, position of the sun, orographic shadows, atmospheric transmission losses and
 282 gains due to scattering, absorption and reflections, multiple reflections between snow and clouds as well as
 283 reflected radiation from snow covered neighbouring slopes. Cloud coverage (when not prescribed) is either
 284 determined by comparing potential to observed global radiation; alternatively, it is estimated using atmospheric
 285 humidity following Liston and Elder (2016). During nighttime either the atmospheric humidity approach is used
 286 or cloudiness is kept constant. In the final step, cloud coverage is spatially interpolated and actual incoming global
 287 radiation is calculated by correcting potential global radiation with cloud coverage for each model grid cell.

288 Reflected short wave radiation depends on surface albedo which strongly varies in space and time, for snow
 289 surfaces mainly depending on grain size. In openAMUNDSEN, albedo is modelled taking into account snow age
 290 and an air temperature-dependent decay function following Rohrer (1992) and Essery et al. (2013):

291
$$\alpha = \alpha_{\min} + (\alpha_{t-1} - \alpha_{\min}) \cdot e^{-\frac{1}{\tau}\delta t}$$

292 where α_{\min} is the (prescribed) minimum albedo, α_{t-1} the albedo in the previous time step, δt the time step length,
 293 and τ is a temperature-dependent recession factor (implemented by prescribing two factors τ_{pos} and τ_{neg} for positive
 294 and negative air or, optionally, surface temperatures). Maximum snow albedo α_{\max} is by default set to 0.85, while
 295 α_{\min} , τ_{pos} , and τ_{neg} are set to 0.55, 200 h, and 480 h. Firn and ice albedo are held constant with $\alpha_{\text{firn}} = 0.4$ and $\alpha_{\text{ice}} =$
 296 0.2 by default. Fresh snow increases albedo, either using a step function – increasing albedo to α_{\max} when a
 297 snowfall above a certain threshold amount per timestep (default: $0.5 \text{ kg m}^{-2} \text{ h}^{-1}$) occurs – or using the continuous
 298 function

299
$$\alpha = \alpha_{t-1} + (\alpha_{\max} - \alpha_{t-1}) \frac{S_f}{S_0},$$

300 where S_f is the snowfall amount and S_0 the snowfall required to refresh albedo (Essery et al., 2013).

301 Incoming longwave radiation from the atmosphere is a function of atmospheric conditions and temperature and is
 302 determined using the Stefan-Boltzmann law. Atmospheric emissivity thereby depends on water vapour content in
 303 clear sky conditions and cloud cover in overcast situations. Additionally, openAMUNDSEN accounts for long-
 304 wave radiation from the neighbouring slopes. Outgoing longwave radiation is calculated following the Stefan-
 305 Boltzmann law with the emissivity of snow and modelled snow surface temperature. The details of the radiation
 306 model follow Corripio (2002) and are described in Strasser et al. (2004).

307 3.5 Precipitation correction

308 Precipitation measurements are vital input for every snow-hydrological model. However, measuring solid
 309 precipitation in complex alpine terrain is prone to large errors which typically results in an undercatch of
 310 precipitation (Rasmussen et al., 2012). This is particularly important for mountain regions with a high amount of
 311 solid precipitation. High wind speeds can cause an undercatch of snowfall up to 50 % (Kochendorfer et al., 2017)
 312 when using typical pluviometers of the Hellmann type. For solid precipitation, different correction methods are
 313 implemented in the model in order to account for the undercatch of precipitation gauges when measuring snow
 314 accumulation. Hanzer et al. (2016) showed that a combination of a weather station-based snow correction factor
 315 taking into account wind speed and air temperature based on an approach by the World Meteorological
 316 Organization (WMO; Goodison et al., 1998) with a subsequent constant post-interpolation additional factor
 317 yielded plausible long-term precipitation amounts. Whereas the first correction is applied for the station recording
 318 amount prior to interpolation to the cells of the rectangular grid, the latter is added to all grid cells of the modelling
 319 domain. Alternatively to the WMO approach, a method which estimates undercatch regardless of precipitation
 320 phase (Kochendorfer et al., 2017) can be selected in the model configuration procedure prior to a model run.

321 3.6 Snow redistribution

322 Irrespective whether rain or snow, with the interpolation scheme in openAMUNDSEN the amount of precipitation
 323 is distributed over the domain depending on the grid cell elevation, the distance of the surrounding weather stations

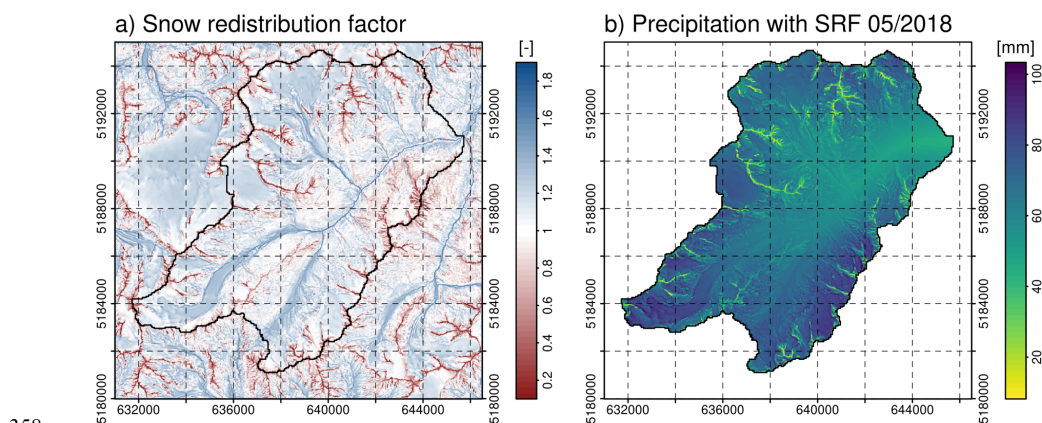


324 and the selected gauge undercatch correction method. The amount of snow at a certain location, however, can be
 325 significantly modified by the lateral processes of preferential deposition, erosion and lateral redistribution. These
 326 processes are driven by wind and gravitational forces (Warscher et al., 2013, Grünewald et al., 2014). Their
 327 consideration is a prerequisite for long-term simulation experiments, because – if neglected – the model will
 328 overestimate snow accumulation on summits and crests, whereas in the depressions beneath it will be
 329 underestimated; as a consequence, also mass balances of existing glaciers in such locations might be wrong due
 330 to not enough mass deposited in the accumulation areas. A recent and comprehensive overview of modelling
 331 lateral snow redistribution is given by Quéno et al. (2023).

332 In openAMUNDSEN a snow redistribution factor (SRF) field can be used to parameterize spatial snow distribution
 333 (figure 5). The SRF describes the fractional amount of snow either eroded or deposited at each pixel location and
 334 modifies the interpolated snowfall field accordingly. Since SRF derivation can depend on various topographic
 335 parameters such as elevation, slope, aspect, curvature, viewshed or terrain roughness, and generally requires site-
 336 specific calibration (Grünewald et al., 2013), openAMUNDSEN allows for flexibility in calculating the SRF field.
 337 It provides functions to compute these topographic parameters but does not prescribe a singular method for final
 338 SRF calculation.

339 Notably, the concept of negative topographic openness (Yokohama, 2002) can be used to parameterize spatial
 340 snow distribution. It is obtained by averaging the nadir angles calculated for all eight compass directions from the
 341 grid point, yielding low values for convex topographic features and high values for concave topographic features.
 342 The openness values finally depend on a length scale which describes the spatial dimension of the given
 343 topographic features affecting the redistribution processes (Helfricht, 2014), resulting in a snow redistribution
 344 factor which describes the fractional amount of snow eroded or deposited for any pixel location. The length scale
 345 thereby depends on the topographic conditions and should therefore be determined for each modelling domain
 346 separately.

347 Effectively, the SRF approach as parameterized in openAMUNDSEN takes into account the processes of
 348 preferential deposition, wind-induced erosion, saltation and turbulent suspension of atmospheric (snow)
 349 precipitation. The way it is implemented in the model does not account for single events, but for their accumulated
 350 effect over longer simulation periods. Such consideration of the snow redistribution processes is required to
 351 prevent artefacts of snow accumulation in long-term simulations, and to produce realistic accumulation and hence
 352 specific mass balances in typical glacier origin areas. In figure 5 an example of a snow redistribution factor field
 353 calculated using a combination of negative openness fields using different length scales (Hanzer et al., 2016) shows
 354 the (red) areas of the summits and ridges where snowfall is significantly reduced, whereas in the slopes and valley
 355 bottoms it is subsequently accumulated (blue areas). Correspondingly, in the presented example the respective
 356 exposed areas receive much less precipitation in May 2018 than the slopes and downvalley areas in the Rofental
 357 (figure 5b).



358

359 Figure 5: The snow redistribution factor (SRF) used in openAMUNDSEN to compensate for snow erosion on
 360 exposed ridges and for snow deposition in the slopes and depressions beneath (a) and an example of monthly total
 361 precipitation with lateral redistribution of snowfall (for May 2018), determined with the snow redistribution factor
 362 (b).



363 Together, three snow amount corrections can be applied in openAMUNDSEN: (i) a windspeed and temperature-
364 dependent precipitation correction at the site of measurement, (ii) an additional post-interpolation factor (see 3.5
365 for a description of how this is modelled), and (iii) the presented adjustment accounting for lateral snow
366 redistribution (as described in 3.6). Whereas (i) and (ii) increase the amount of measured precipitation towards a
367 more realistic volume all over the entire grid, (iii) solely redistributes the solid amount of precipitation from areas
368 of erosion to areas of deposition.

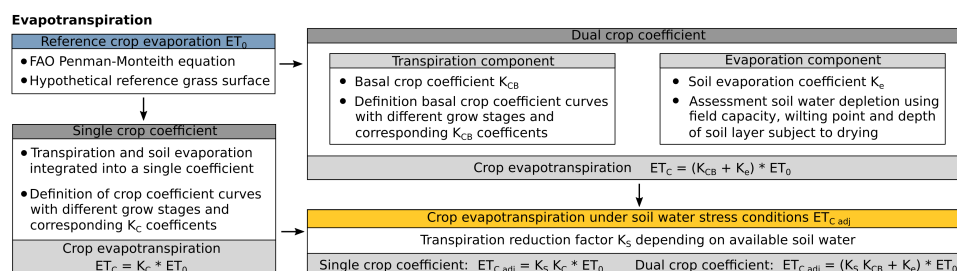
369 3.7 Snow-canopy interaction

370 Forest canopies generally lead to a reduction of global radiation, precipitation and wind speed at the ground,
371 whereas humidity and long-wave radiation are increased and the diurnal temperature cycle is dampened. In
372 openAMUNDSEN, the micrometeorological conditions for the ground beneath a forest canopy are derived from
373 the interpolated measurements (assuming the weather stations are located in the open) by applying a set of
374 modifications for these meteorological variables. The modifications are based on the effective Leaf Area Index
375 (LAI) of the trees composing the stands, i.e. the sum of the classical LAI and the Cortex Area Index CAI (Strasser
376 et al., 2011). By means of the modified meteorological variables, the processes of interception, sublimation,
377 unloading by melt and fall down by exceeding the canopy snow-holding capacity are calculated. Liquid
378 precipitation is assumed to fall through the canopy and is added to the ground snow cover (see figure 1d).

379 Simulations with the snow-canopy interaction model for an idealized mountain (Strasser et al., 2011) showed that,
380 despite reduced accumulation of snow on the ground beneath the trees, both rates and seasonal totals of sublimation
381 of snow previously intercepted in a canopy were significantly higher than the sublimation losses from the ground
382 snow surface. On top of that, shadowing leads to reduced radiative energy input inside the canopy and hence
383 protection of the snow. The type of forest, exposition, the specific meteorological conditions and the general
384 evolution of the winter season play an important role as well: during winter, the effect of reduced accumulation is
385 dominant, whereas during spring, the shadowing effect with reduced ablation prevails. In winters with much snow,
386 the effect of shadowing by the trees dominates and snow lasts longer inside the forest than in the open. In winters
387 with little snow, however, the sublimation losses of snow are dominant and the snow lasts longer in open areas.
388 This might vary, however, for northern and southern exposure to radiation and time of the year due to the strong
389 effect of solar radiation on melt. In early and high winter, the radiation protection effect of shadowing is small. An
390 intermittent melt out of the snow cover beneath the trees can occur if little snow is available. The shadowing effect
391 becomes more efficient and snowmelt is delayed relative to nonforested areas in late winter and spring. Due to the
392 combination of all these processes, the modelling of snow-canopy interaction can lead to complex and very
393 heterogeneous patterns of snow coverage and duration in alpine regions with forest stands (Essery et al., 2009;
394 Rutter et al., 2009; Strasser et al., 2011).

395 3.8 Crop evapotranspiration

396 For non-snow-covered surfaces the actual evapotranspiration of vegetated areas is calculated using the FAO
397 Penman-Monteith approach (Allen et al., 1998), for which a schematic overview is illustrated in figure 6. In a first
398 step, the evapotranspiration is calculated for a reference crop (grass) using the meteorological variables and a
399 limiting amount of available water in the soil storage. In forested areas, thereby the inside-forest meteorological
400 conditions are considered. Then, the resulting evapotranspiration is modified according to the vegetation type
401 using particular crop coefficients which integrate the effects of plant height, albedo, stomata resistance and
402 exposed soil fraction. Crop coefficients are available for a wide range of plant types in the given literature and
403 change their value along the season according to predefined growth stage lengths. For each plant type,
404 evapotranspiration can either be calculated using a single-coefficient approach which integrates the effects of crop
405 transpiration and soil evaporation into a single coefficient, or using a dual-coefficient approach which considers
406 crop transpiration and soil evaporation separately. Soil evaporation is computed considering the cumulative depth
407 of water evaporated from the top soil layer and the fraction of the soil surface that is both exposed and wetted. The
408 soil type determines the amount of evaporable amount of water with respect to field capacity, water content at
409 wilting point and depth of the surface soil layer that is subject to drying by means of evaporation (0.10 to 0.15 m);
410 parameters are available for sand, loamy sand, sandy loam, loam, silt loam, silt, silt clay loam silty clay and clay
411 (Allen et al., 1998). With this approach the water balance of the upper soil layer is computed, determining if surface
412 runoff and deep percolation can occur or if evapotranspiration is limited. If the evapotranspiration module is
413 activated, both soil types and land cover must be available as maps.



414

415 Figure 6: Schematic overview of the FAO evapotranspiration module to compute the water flux from the soil
 416 through the plants to the atmosphere with the Penman-Monteith equation. Fluxes are calculated for a reference
 417 crop and then scaled to other landuse classes.

418 3.9 Layering schemes

419 In openAMUNDSEN two different layering schemes for snow- or ice-covered surfaces are implemented (figure
 420 1c). The “cryospheric layer version“ parameterizes layers of new snow, old snow, firn and glacier ice. The
 421 advantage of using these layers is that they are distinctively different in their optical properties; their surfaces can
 422 be recognized and distinguished by humans in the field or on photographs, or by satellites with sensors sensitive in
 423 the visible range of the spectrum. The model tracks the thickness of these layers and parameterizes their density
 424 with more or less empirical relations. For the ground interface a fix upwards heat flux can be set (usually 2 W m^{-2}
 425 in the Alpine region). The most comprehensive descriptions of this model versions can be found in Strasser
 426 (2008), Strasser et al. (2011) and Hanzer et al. (2016).

427 The “multi-layer version“ is adopted following the structure of the FSM model (Essery, 2015). It considers a
 428 number of layers (by default three) with fixed maximum depths (for the upper two ones), all of them without
 429 physical representation. In this model version the fluxes of mass and energy are tracked by means of an iterative
 430 computation of the state variables temperature and liquid water content such that the balances of mass and energy
 431 are closed for each layer. The energy transfer at the snow-soil interface is calculated by means of a 4-layer soil
 432 model. A detailed description of the implemented multi-layer model scheme can be found in Essery (2015).

433 Whereas the cryospheric layer version of openAMUNDSEN can be combined with both the simple or the enhanced
 434 temperature-index approach or, alternatively, with the energy balance method, the multi-layer version requires the
 435 energy balance method to compute the energy and mass balances of the surface and the snow layers beneath (see
 436 figure 1c). The simulation of glacier evolution as a response to the climatic conditions requires the cryolayer
 437 version to be applied.

438 3.9.1 Cryospheric layer version

439 In the cryospheric layer version of openAMUNDSEN, the transitions between new snow and old snow occur when
 440 reaching a predefined snow density threshold (by default 200 kg m^{-3}), while remaining snow amounts at the end
 441 of the ablation season (by default 30 September) are transferred to the firn layer. Compaction for the new and old
 442 snow layers is calculated using the methods described below (in 3.10); for firn a linear densification is assumed.
 443 Once reaching a threshold density of 900 kg m^{-3} , firn is added to the ice layer beneath. While snow albedo is
 444 parameterized using the aging curve approach (Rohrer, 1992), firn and ice albedo is kept constant (with default
 445 values of 0.4 and 0.2, respectively). The details of the cryospheric layer version of openAMUNDSEN are best
 446 described in Hanzer et al. (2016).

447 While snow temperature of the individual layers is not calculated using the cryospheric layering scheme, an
 448 approach following Braun (1984) and Blöschl and Kimbauer (1991) is applied in order to determine an average
 449 cold content of the snow layers. This cold content builds up when the snowpack cools; it has to be depleted before
 450 melt and subsequent runoff can occur at the snowpack bottom. The maximum possible cold content is thereby set
 451 to 5 % of the total snowpack weight (the latter can be converted to an energy by multiplication with the latent heat
 452 of fusion).



453 When using this scheme, the snowpack is taken as a bulk layer to solve the surface energy balance. If air
454 temperature is above 0 °C the model assumes that the snow surface temperature is 0 °C and melt occurs, the
455 amount of which can be computed from the available excess of the energy balance. If the air temperature is below
456 0 °C, an iterative procedure to compute the snow surface temperature for closing the energy balance is applied.
457 With this procedure, the snow surface temperature is altered until the residual energy balance passes zero.

458 3.9.2 Multi-layer version

459 In the multi-layer version of openAMUNDSEN, the vertical heat fluxes are computed through both the snow pack
460 and the ground (Essery, 2015). To solve the energy balance, melt is first assumed to be zero for the surface
461 temperature change of every timestep. Snow is melting if the energy balance results in a surface temperature
462 passing 0 °C. The temperature increment is recalculated assuming that all of the snow melts; if this results in a
463 surface temperature below 0 °C, snow only partially melts during the timestep (Essery, 2015). Snow layer
464 temperatures are then updated using an implicit finite difference scheme. Snow compaction and density of each
465 layer are calculated in the same way as for the cryospheric layer version, as described in the following.

466 3.10 Snow density

467 For both layering schemes, fresh snow density is calculated using the temperature-dependent parameterization by
468 Anderson (1976), assuming a minimum density of 50 kg m⁻³. Snow compaction can be calculated using two
469 methods, one physically based approach following Anderson (1976) and Jordan (1991), and one empirical
470 approach following Essery (2015). For the former, density changes are calculated in two stages due to snow
471 compaction and metamorphism, taking into account temperature and snow load imposed by the layers above (see
472 also Koivusalo et al., 2001). For the empirical method, assumptions are made for maximum density of snow below
473 0 °C and for melting conditions (default values: 300 kg m⁻³ for cold snow and 500 kg m⁻³ for melting snow). The
474 timescale for compaction is an adjustable parameter (default value: 200 h). The increase of density for every
475 timestep is calculated as a fraction of the compaction timescale multiplied with the difference of maximum density
476 and the density of the last timestep (Essery, 2015).

477 3.11 Liquid water content

478 Meltwater occurring at the snow surface is not immediately removed from the snowpack, but a certain liquid water
479 content (LWC) can be retained. Following either Braun (1984) or Essery (2015), the maximum LWC is defined
480 as mass fraction of SWE or as a fraction of pore volume that can be filled with liquid water (volumetric water
481 content). If the maximum LWC is reached during snowmelt, runoff at the bottom of a snow layer occurs and drains
482 to the snow layer underneath, or – for the bottom snow layer – into the upper soil layer respectively. In the case of
483 a negative energy balance, this liquid water can refreeze.

484 3.12 Snowmelt

485 Snowmelt can be computed in openAMUNDSEN by several approaches with different complexity. The simplest
486 method, the classical temperature index approach, is particularly suited for regions where only daily recordings of
487 temperature and precipitation are available. Melt M in mm per timestep is thereby computed as:

$$488 \quad M = \begin{cases} \text{DDF} \cdot T & T > T_T \\ 0 & T \leq T_T \end{cases}$$

489 with DDF being the degree day factor (or melt coefficient) in mm w.e. °C day⁻¹ and T the mean daily temperature
490 in °C. T_T is the threshold temperature above which melt is assumed to occur (e.g., 1 °C). Low DDFs will be
491 obtained for cold and dry areas, whereas high DDFs can be expected for warm and wet areas.

492 Second is a hybrid approach between the temperature index method and the energy balance, the so-called
493 "enhanced temperature index method" by Pellicciotti et al. (2005). By including potential shortwave radiation and
494 albedo these computations can be applied to meteorological variables in hourly time steps:

$$495 \quad M = \begin{cases} \text{TF} \cdot T + \text{SRF} \cdot (1 - \alpha) \cdot G & T > T_T \\ 0 & T \leq T_T \end{cases}$$

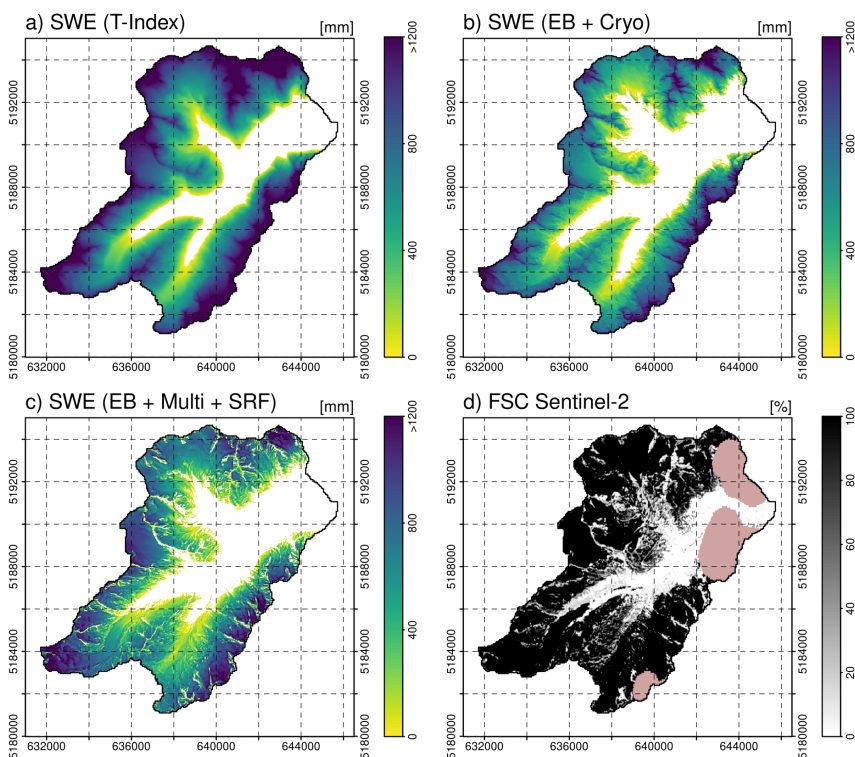


496 where T is an hourly temperature in $^{\circ}\text{C}$, α is albedo and G is potential incoming shortwave radiation (which is
 497 simulated as described in 3.4). TF and SRF are two empirical coefficients, the temperature factor and the shortwave
 498 radiation factor, expressed in $\text{mm h}^{-1} \text{ }^{\circ}\text{C}^{-1}$ and $\text{m}^2 \text{ mm W}^{-1} \text{ h}^{-1}$. T_T is equal to $1 \text{ }^{\circ}\text{C}$. When temperature is below T_T
 499 no melt occurs.

500 Melt rates using either the cryospheric layer or the multi-layer version of openAMUNDSEN also can be computed
 501 using the surface energy balance equation:

$$502 \quad Q + H + E + A + B + M = 0$$

503 with Q being the shortwave and longwave radiation balance, H the sensible heat flux, E the latent heat flux, A the
 504 advective energy supplied by solid or liquid precipitation and B the soil heat flux. M is the energy potentially
 505 available for melt. For a detailed description of the calculation of the individual energy fluxes see Strasser (2008).
 506 A comparison of modelling results achieved with the different approaches is shown in figure 7. The temperature
 507 index approach delivers results which only show dependence on the temperature and the precipitation gradient,
 508 but no pattern affected by different radiative energy input depending on slope and aspect (figure 7a). These
 509 computations can be performed with daily time step, hence they are comparably fast and only require temperature
 510 and precipitation as meteorological input variables. Using the energy balance for computation of the accumulation
 511 and ablation processes at the snow surface, and the cryolayer version for the internal processes inside the snow
 512 pack, leads to a significantly more differentiated pattern of snow distribution (figure 7b): The result clearly shows
 513 the effect of topography on the ablation pattern of the snow cover on this day. In figure 7c, the energy balance was
 514 combined with the multi-layer version of the model and the application of the SRF to consider the lateral snow
 515 redistribution processes. Now, erosion from exposed summit and ridge areas can be detected, as well as additional
 516 accumulation in the slopes beneath. This complex pattern best matches the snow distribution on this particular day
 517 as depicted in the fractional snow cover map derived from a Sentinel-2 image captured on the same day (figure
 518 7d).



519

520 Figure 7: Snow water equivalent on 18/06/2019 in the Rofental, simulated using the T-Index approach in daily
 521 resolution without wind-induced snow redistribution (a), the energy balance approach and cryospheric layers



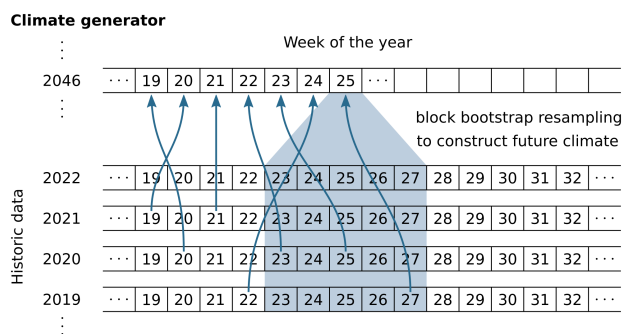
522 without wind-induced snow redistribution (b), the energy balance approach with multi-layers including wind-
 523 induced snow redistribution (c). Panel (d) shows a fractional snow cover map based on Sentinel-2 satellite data
 524 for the same day.

525 4 Generation of potential future climate

526 Future scenarios of climate can be produced by means of a stochastic "block bootstrap resampler" (Mauser et al.,
 527 2007) which is realized in a pre-processing routine for openAMUNDSEN. The method requires a sufficiently long
 528 time series of meteorological recordings from a period with highly variable weather conditions in the considered
 529 region. The principles of the implemented weather generator follow Strasser (2008) and are described herein. The
 530 basic assumption of the method is that a climate storyline can be divided into time periods which are characterized
 531 by a certain mean temperature and precipitation and that these two variables are not independent from each other:

532
$$P_{\text{tot}} = f(T_{\text{mean}})$$

533 P_{tot} is the total precipitation amount of a specific time period, T_{mean} is the mean temperature and f their functional
 534 dependency. The time periods can be set to any length, i.e. to months as in Mauser et al. (2007) or to weeks as in
 535 Strasser (2008). In a first step, the typical annual course of the measured meteorological variables is constructed
 536 by computing mean temperature and total precipitation for the periods using all years of the historical dataset and
 537 applying the given formula. Whereas temperature is characterized by a typical seasonal course in the Alpine region
 538 (warm in summer, cold in winter), the annual course of the precipitation totals of a period with certain duration
 539 can be more complex. The resulting mean annual climate course is used to construct the future data time series
 540 period by period: firstly, the respective temperature for the period is modified with a random variation factor and
 541 an assumed projected trend (e.g., as suggested from a regional climate model). Then a corresponding precipitation
 542 is derived and, again, a random variation. In the end the climate of a future period is defined by the so obtained
 543 mean temperature and precipitation. In a final step, the period from the historical pool having the most similar
 544 temperature and precipitation is selected by applying an Euclidian nearest neighbour distance measure. All
 545 respective data of the chosen period (e.g., air temperature, precipitation, global radiation, relative humidity and
 546 wind speed) are then added to the future time series to be constructed. This procedure is repeated for all periods
 547 of the year, and for all years of the future time series. By modifying the applied random variation a change in
 548 climate variability can be simulated. To allow for more flexibility in the construction of the periods, in our
 549 implementation the basic population from which the measured period is chosen (= the number of periods available,
 550 being equal to the number of years for which observational data is available) can be synthetically extended by
 551 allowing for one or more periods before and after the one to be constructed (figure 8).



552
 553 Figure 8: openAMUNDSEN pre-processing with the climate generator: choice of corresponding historic periods
 554 to construct a future climate data set with preset trend and random variation from given meteorological
 555 observations. The number of periods from which data can be selected to construct a particular period of a year in
 556 the future time series is set to three in this example.

557 The described procedure has a number of specific features: (i) the key advantage of the method is that the physical
 558 relationship between the meteorological variables is maintained in the simulation; (ii) bootstrap models obviously
 559 work well at high temporal resolution, e.g. 1 to 3-hourly; (iii) the produced data time series is in the validated
 560 range for the hydrological modelling; (iv) a synthetic baseline scenario can easily be constructed by assuming a
 561 zero trend for temperature; (v) the procedure is computationally very efficient and (vi) finally, the spatial
 562 resolution of the data is preserved as it exactly corresponds to the weather station locations. However, a significant



563 drawback of the method is that auto-correlation between the periods is lost and the consideration of changes in the
564 variability of the meteorological variables is limited. Together with the fact that changes in extreme values are not
565 considered (only their frequency can change) it becomes clear that the data resulting from the method cannot be
566 used for modelling variations in the extent of hydrological extremes. Furthermore and most crucial, no coupling
567 is considered between the (simulated) characteristics of the land surface – e.g. whether it is snow-covered or not
568 – with the atmosphere, and therefore the important effects of feedback mechanisms are not conserved in the
569 construction of the future dataset. This, however, is a drawback that also many physical climate models share.

570 5 Implementation in Python

571 For the rewriting of the original AMUNDSEN IDL code the Python language was chosen due to its popularity,
572 simplicity and the large number of excellent and well-tested numerical and scientific libraries available.
573 openAMUNDSEN especially makes use of the packages NumPy (Harris et al., 2020) for array calculations, pandas
574 (McKinney, 2010) and Xarray (Hoyer and Hamman, 2017) for processing time series and multidimensional data
575 sets. While Python, being a scripting language, has limitations in terms of execution performance, these libraries
576 allow efficient code execution due to the use of Fortran or C for the underlying calculations. For increasing the
577 runtime efficiency of performance-critical functions within openAMUNDSEN, the Numba library (Lam et al.,
578 2015) is furthermore used for dynamically translating Python code to machine code.

579 openAMUNDSEN is implemented using an object oriented architecture, centering around the `OpenAmundsen`
580 class as the primary interface. This class represents a single model run and encapsulates all methods required to
581 initialize and run the model. openAMUNDSEN can either be used as a stand-alone utility (using the
582 `openamundsen` command line tool) or as a Python library. When used in stand-alone mode, the
583 `openamundsen` command line tool must be invoked with the name of a configuration file in YAML format (i.e.,
584 `openamundsen config.yml`). If used as a library from within a Python script, the model configuration in
585 form of a Python dictionary (commonly again sourced from a YAML file) must be passed when instantiating an
586 `OpenAmundsen` object. A typical model run executed from within Python looks as follows (see also figure 8):

```
587 import openamundsen as oa  
588  
589 config = oa.read_config('config.yml')  
590 model = oa.OpenAmundsen(config)  
591 model.initialize()  
592 model.run()
```

593 This allows for substantial flexibility in simulation preparation, execution and postprocessing. For example:

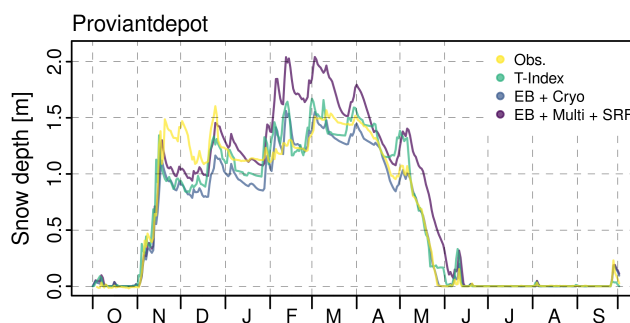
- 594 • It is possible to change the model state variables after initializing them (e.g., the snow layers – which are by
595 default initialized as being snow-free – can be initialized using prepared snow depth or SWE data). This is
596 not only possible prior to running the model, but can also be done at any point during the model run by using
597 `model.run_single()` – which performs the calculations for a single time step – in a loop, instead of the
598 `model.run()` call
- 599 • Model results do not necessarily have to be written to file but can also be stored in-memory and accessed
600 directly from the `OpenAmundsen` class instance for further processing
- 601 • Several model runs can be prepared in a single script (by initializing multiple `OpenAmundsen` instances)
602 and, e.g., be run in parallel.

603 Model runtime is influenced by various factors, most importantly the number of pixels simulated, but also the
604 number of weather stations used for interpolation of the meteorological variables, the choice of the layering scheme
605 (cryospheric layers vs. multi-layer), the activated submodules (snow-canopy interaction, evapotranspiration, etc.),
606 the amount of I/O operations (the number of output variables and the temporal frequency in which they are written
607 to file), and others. openAMUNDSEN generally leverages multiple CPU cores (by operating over the model grid
608 pixels in parallel using Numba's parallelization features), however in practice the speedup gained by parallelism
609 is small due to the short-lived nature of the respective functions and the overhead from scaling to multiple cores.
610 To give an example, a point-scale (i.e., 1x1) model run completes a full-year simulation using hourly time steps
611 in approx. 2 minutes on an AMD EPYC 7502P processor. A spatially distributed model run for a medium-sized
612 model grid (450 x 650 pixels) requires approx. 36 minutes per simulation year in single-core mode, and
613 33/30/28/27 minutes when using 2/4/8/16 cores, respectively. Running the model in pure Python mode (i.e.,
614 disabling the Numba just-in-time compilation) can increase runtime by a factor of more than 40.



615 6 Model uncertainty and evaluation

616 The original versions of ESCIMO and then AMUNDSEN have been extensively validated in various Alpine sites
617 (Strasser and Mauser, 2001; Strasser et al., 2002; Strasser, 2004; Pellicciotti et al., 2005; Strasser et al., 2008;
618 Strasser, 2008; Hanzer et al., 2014; Marke et al., 2015). Hanzer et al. (2016) showed the uncertainty of the model
619 application by means of a systematic, independent, complete and redundant validation procedure based on the
620 observation scale of temporal and spatial support, spacing, and extent (Blöschl, 1999). To evaluate the dimensions
621 of the observation scale a comprehensive set of eight independent validation sources was used: (i) mean areal
622 precipitation derived by conserving mass in the closure of the water balance, (ii) time series of snow depth
623 recordings at the plot scale, (iii-iv) multitemporal snow extent maps derived from Landsat and MODIS satellite
624 data products, (v) snow accumulation distribution derived from airborne laser scanning data, (vi) specific surface
625 mass balances for three glaciers in the study area, (vii) spatially distributed glacier surface elevation changes for
626 the entire area and (viii) runoff recordings for several subcatchments. The results indicate a high overall model
627 skill in all the dimensions and confirmed the very good model evaluations of the published case studies (Hanzer
628 et al., 2016). As an example for the model performance at the location of a meteorological station, figure 9 shows
629 snow depth simulation results achieved with meteorological observations at the Proviantdepot station (2737 m
630 a.s.l.) compared to recordings of snow depth for the season 2019 to 2020. Despite the missed significant snowfall
631 event at the beginning of the season, all model version well capture the seasonal course of the snow depth
632 evolution. The temperature index version could be optimized by means of calibration to better match the meltout
633 time, so the lag of some days is not a lack of model “accuracy” in this case (a standard degree day factor of 9.5
634 mm K⁻¹ d⁻¹ was used, the same as for the results in figure 7a, without further calibration). Both energy balance
635 versions of the model well represent the observations.



636

637 Figure 9: Observed and simulated snow depth at the location of the meteorological station Proviantdepot (2737 m
638 a.s.l.) located in the area of the example application Rofental for the winter season 2019/2020.

639 For the multi-layer version of the openAMUNDSEN model, the uncertainty of the model simulations was
640 investigated by Günther et al. (2019) for point simulations at the local scale and by Günther et al. (2020) for
641 distributed applications.

642 openAMUNDSEN was also subject to several model intercomparison studies. The very first version of the bulk
643 energy balance approach of AMUNDSEN (then called ESCIMO) was compared to CROCUS for data of the Col
644 de Porte weather station located in the French Alps (1340 m a.s.l.) (Strasser et al., 2002). Later, the model was
645 intercompared to many other snow models in the series of the international Snow Model Intercomparison Projects
646 (SnowMIPs): in the original SnowMIP project (Etchevers et al., 2004), ESCIMO was evaluated together with 22
647 other snow models of varying complexity at the point scale using meteorological observations from the two
648 mountainous Alpine sites Col de Porte (1340 m a.s.l.) and Weissfluhjoch (2540 m a.s.l.), both in the European
649 Alps. In the follow-up project SnowMIP2 (<https://www.geos.ed.ac.uk/~ressery/SnowMIP2.html>; last access:
650 March 7, 2024), thirty-three snowpack models of varying complexity and purpose were evaluated across a wide
651 range of hydrometeorological and forest canopy conditions at five Northern Hemisphere locations, namely Alptal
652 (Switzerland; 1185 m a.s.l.), BERMS (Canada; 579 m a.s.l.), Fraser (USA; 2820 m a.s.l.), Hitsujigaoka (Japan;
653 182 m a.s.l.) and Hyytiälä (Finland; 181 m a.s.l.) (Essery et al., 2009; Rutter et al., 2009). For each location two
654 sites were used, one in the open (no canopy) and one forested (canopy) site. Finally, the surface energy-balance
655 core of the model participated in ESM-SnowMIP (<https://climate-cryosphere.org/esm-snowmip/>; last access:
656 March 7, 2024), an international intercomparison project to evaluate twenty-seven current snow models against
657 local and global observations for a wide variety of settings, including snow schemes that are included in Earth



658 System Models (Krinner et al., 2018). A further objective of ESM-SnowMIP is to better quantify snow-related
659 feedbacks in the Earth system. ESM-SnowMIP is tightly linked to the Land Surface, Snow and Soil Moisture
660 Model Intercomparison Project (<https://climate-cryosphere.org/ls3mip/>; last access: March 7, 2024), which is a
661 contribution to the 6th phase of the Coupled Model Intercomparison Project (CMIP6; <https://wcrp-cmip.org/cmip-phase-6-cmip6/>; last access: March 7, 2024). One of the results of ESM-SnowMIP was an unexpected surprise:
662 more sites, more years and more variables do not necessarily provide more insight into key snow processes;
663 instead, "this led to the same conclusions as previous MIPs: albedo is still a major source of uncertainty, surface
664 exchange parameterizations are still problematic, and individual model performance is inconsistent. In fact, models
665 are less classifiable with results from more sites, years and evaluation variables" (Menard et al., 2021). Currently,
666 openAMUNDSEN belongs to the range of models within the COPE initiative (Common observation period
667 experiments) of the INARCH project (<https://inarch.usask.ca/science-basins/cope.php>; last access: March 7 2024).
668 It can be expected that manyfold new insights about the models internals will mutually be learned from these
669 model intercomparisons in the near future.
670

671 7 Conclusions

672 In this paper, we present openAMUNDSEN, a fully distributed open source snow-hydrological model for
673 mountain catchments. The model includes a wide range of process representations of empirical, semi-empirical
674 and physical nature. openAMUNDSEN allows to find a compromise between temporal and spatial resolution, time
675 span of the simulation experiment, size of the considered region, physical detail and consistency as well as
676 performance. E.g., it offers to choose between the temperature index approach to determine snowmelt rates from
677 daily temperature and precipitation, or hourly closure of the surface energy balance and calculation of a number
678 of state variables for several snow layers using temperature, precipitation, humidity, radiation and wind speed as
679 forcing data. openAMUNDSEN is computationally efficient, of modular nature, easily extendible and also allows
680 for using factorial designs to determine interactions between processes and their effect on the accuracy of the
681 simulation results (Essery et al., 2013; Günther et al., 2019, 2020). Hence, the application of the model is very
682 flexible and it supports a multitude of applications or simulation experiments to address any kind of hydrological,
683 glaciological, climatological or related research questions.

684 The model has been evaluated and proven its applicability at many sites worldwide. Most of all, it was subject to
685 a systematic, innovative, multilevel spatiotemporal validation with independent datasets of various resolution and
686 extent from a site in the European Alps (Hanzer et al., 2016). In all cases, the model showed high overall skill and
687 well captured the spatial and temporal patterns as well as magnitudes of the observations.

688 The Python model code described here is available for the public in Hanzer et al. (2023) and also available as open
689 source project on GitHub (<https://github.com/openamundsen/openamundsen>; last access: March 7, 2024),
690 including a documentation which is subject to continuous extension and improvement (<https://doc.openamundsen.org>;
691 last access: March 7, 2024). The climate generator is available at
692 <https://github.com/openamundsen/openamundsen-climategenerator> (last access: March 7, 2024).

693 8 Future developments

694 The openAMUNDSEN model code is continuously further improved and extended. The modelling of the
695 processes of lateral snow redistribution will benefit from a simulation of local wind fields, e.g. as recently
696 demonstrated by Quéno et al. (2023). On top of the wind-induced processes of saltation, turbulent suspension (with
697 sublimation) snow is also transported downslope by means of avalanches, the origin also of accumulated masses
698 of snow leewards of crests. In the original, IDL-based version of AMUNDSEN (Strasser, 2008) the avalanche
699 process has been parameterized based on the Mflow-TD algorithm by Gruber (2007); the latter was later extended
700 with a continuous update of the surface model to correct for eroded/deposited masses of snow (Bernhardt and
701 Schulz, 2010). A comparable algorithm is in development to be included in openAMUNDSEN soon. Another path
702 of improvement is foreseen for the snow-canopy interaction module. On the one hand, the parameterization of
703 inside-canopy meteorological variables derived from measurements taken in the open will be further improved by
704 utilizing the new (winter) measurements of inside-canopy meteorological variables, i.e. from the Col de Porte
705 meteorological station in the French Alps (Sicart et al., 2023). Further, it is intended to couple the snow-canopy
706 interaction module with dynamically simulated evolutions of the LAI from iLand simulations (Seidl et al., 2012).
707 The ultimate goal of this effort is to bi-directionally couple the snow processes inside the canopy with its long-
708 term evolution to enable the simulation of scenarios of the effect of climate change on the coupled
709 hydrological/biological system of mountain forests.



710 To compute streamflow discharge in mostly glacierized catchment to be compared to gauge recordings, a linear
711 reservoir cascade approach following Asztalos (2007) has been implemented as a separate post-processing tool
712 (Hanzer et al., 2016). The linear reservoir approach is a comparable simple empirical method to produce a runoff
713 curve for a certain location of the stream without the need to provide physical parameters for the catchment
714 characteristics (e.g., soil), or the wave propagation along the channel. Instead, a series of parallel linear reservoir
715 cascades (Nash, 1960) is computed the parameters of which are calibrated by maximizing the Nash-Sutcliffe
716 efficiency NSE and minimizing the relative volume error (following Lindström, 1997). Due to its purely empirical
717 nature and the fact that its application is limited to small glacierized catchments only, the linear reservoir approach
718 will not be included into the openAMUNDSEN project on the openAMUNDSEN GitHub repository. Instead, it is
719 foreseen to test and develop new approaches in machine learning, e.g. in the field of LSTM (Long Short-Term
720 Memory Networks Modelling) which can provide very good results for hydrological streamflow simulations
721 (Kratzert et al., 2021). Other promising new developments also exist in the combination of hydrological modelling,
722 remote sensing and machine learning (De Gregorio et al., 2019a and b). Since AI is a field of rapid development
723 in scientific modelling we expect significant advances also in snow-hydrological modelling using these innovative
724 methods.

725 *Code availability.*

726 The openAMUNDSEN model code is available under the MIT license, a short and simple permissive license with
727 conditions only requiring preservation of copyright and license notices. The model in the presented version v0.8.3
728 is available on Zenodo (Hanzer et al., 2023). The GitHub download site for the model code is
729 <https://github.com/openamundsen/openamundsen> (last access: March 7, 2024).

730 *Data availability.*

731 We provide a comprehensive data set that can be used with openAMUNDSEN for the high alpine research
732 catchment of the upper Rofenache (98.1 km², Ötztal Alps, Tyrol/Austria) including (i) glaciological data, i.e.,
733 recordings of glacier volume and geometry changes; (ii) meteorological data as recorded by temporally installed
734 or permanent automatic weather stations; (iii) hydrological data characterizing the water balance of the respective
735 glaciated (sub-) catchment; and (iv) airborne and terrestrial laser scanning data (Strasser et al. 2018). The data time
736 series cover periods of various lengths until 2017. This data has been extended until August 2023 under the same
737 license (Warscher et al., 2024).

738 *Sample availability.*

739 The sample data for the Rofental research catchment (Ötztal Alps, Austria) which has been used to produce the
740 figures [is](#) described in Strasser et al. (2018) and Warscher et al. (2024).

741 *Author contributions.*

742 US designed and developed the original version of the AMUNDSEN model and wrote the paper manuscript; MW
743 did many model experiments, wrote the documentation, further develops the model, processes the Rofental data,
744 supports the maintenance of the GitHub site and contributed to the final version of the manuscript; ER supported
745 the example application model simulations and the manuscript writing process, produced the figures and
746 contributes to further model development; FH developed many parts of the model in the IDL version, designed
747 and implemented the new Python version, continuously further develops the model, supervises the GitHub
748 repository and any improvement there as well as wrote the technical parts of the manuscript of this paper.

749 *Competing interests.*

750 The authors declare that no competing interests exist.

751 *Acknowledgements.*

752 Since the beginning of the AMUNDSEN model development, many colleagues have contributed with the valuable
753 experience in field work, modelling and programming. In the early days, the basics for the general design of such
754 a model were learned from Wolfram Mauser (University of Munich, Germany), and in particular for anything
755 snow-specific from “Wasti” Markus Weber, Heidi Escher-Vetter and Ludwig Braun (Bavarian Academy of
756 Sciences Munich, Germany) as well as from Michael Kuhn (University of Innsbruck, Austria). Later, the model
757 code was further developed using the valuable experiences from a 1-year-position of visiting scientist at the Centre



758 d'Etudes de la Neige in Grenoble, France. There, the model mostly profited from the lessons learned from Yves
759 Lejeune, Pierre Etchevers † and Eric Martin, as well as from the colleagues of the crew at the snow research center
760 in 1999/2000. At CEN, the first author learned a lot about snow processes and their modelling from first hand of
761 the professionals. The Arolla glacier expedition 2001, with a lot of joint learning success, was supported by Paolo
762 Burlando, Francesca Pellicciotti and Martin Funk (all ETH Zurich), Javier Corripio (University of Edinburgh,
763 Scotland) and Ben Brock (University of Dundee, Scotland). Ongoing testing, improvements as well as support for
764 further model development in several projects and publications was contributed by Monika Prasch and Matthias
765 Bernhardt (both University of Munich, Germany) as well as Thomas Marke (University of Innsbruck, Austria).
766 The model development also significantly profited from the support of the Berchtesgaden National Park
767 administration, namely Michael Vogel, Helmut Franz and Annette Lotz (Berchtesgaden, Germany). Many field
768 work experiences by Stefan Pohl † and Jakob Garvelmann helped to improve the process descriptions for the forest
769 canopy module. In general, by many provided opportunities in joint projects, the openAMUNDSEN model
770 development generally profited from the work of Samuel Morin (Meteo-France, Grenoble, France), Richard
771 Essery (University of Edinburgh, Scotland), Glen E. Liston (Cooperative Institute for Research in the
772 Atmosphere/Fort Collins, Colorado) and John Pomeroy (University of Saskatchewan, Canada). The LTSER
773 platform Tyrolean Alps – which the Rofental site belongs to – is part of the national and international long term
774 ecological research network LTER-Austria, LTER Europe and ILTER. This infrastructure is financially supported
775 by the University of Innsbruck (Faculty of Geo- and Atmospheric Sciences); it is part of its Research Area
776 “Mountain Regions”. The University of Innsbruck generously supported the complete re-design and programming
777 of the model in Python and hence the possibility to provide it as open source code to the scientific community.
778 Finally, the University of Innsbruck also gratefully supported the open access publication of this paper.

779



780 References

- 781 Allen, R. G., Pereira, L. S., Raes, D. and Smith, M.: Crop evapotranspiration - Guidelines for computing crop
782 water requirements. FAO Irrigation and Drainage Paper No. 56, FAO 1998, 174 p. ISBN 92-5-104219-5,
783 <https://www.fao.org/3/x0490e/x0490e00.htm>, 1998.
- 784 Anderson, E. A.: A point energy and mass balance model of a snow cover (NOAA Technical Report NWS 19, pp.
785 1–172). NOAA, <https://repository.library.noaa.gov/view/noaa/6392>, 1976.
- 786 Asztalos, J., Kirnbauer, R., Escher-Vetter, H. and Braun, L.: A distributed energy balance snowmelt model as a
787 component of a flood forecasting system for the Inn river. In: Strasser, U. and Vogel M. (eds.) (2008): Proceedings
788 of the Alpine*Snow*Workshop, Munich, October 5–6, 2006, Germany. Research report 53, ISBN13 978-3-
789 922325-60-4, National Park Berchtesgaden, 2007.
- 790 Bavay, M. and Egger, T.: MeteoIO 2.4.2: a preprocessing library for meteorological data. *Geosci. Model. Dev.*
791 *Vol. 8*, pp. 3135–3151, <https://doi.org/10.5194/gmd-7-3135-2014>, 2014.
- 792 Bernhardt, M. and Schulz, K.: SnowSlide: A simple routine for calculating gravitational snow transport. *Geophys.*
793 *Res. Lett.*, *Vol. 37*, L11 502, <https://doi.org/10.1029/2010GL043086>, 2010.
- 794 Blöschl, G.: Scaling issues in snow hydrology: *Hydrol. Process.*, *Vol. 13*, 2149–2175, 1999.
- 795 Blöschl, G. and Kirnbauer, R.: Point snowmelt models with different degrees of complexity—internal processes. *J.*
796 *Hydrol.*, *Vol. 129*, pp. 127–147, [https://doi.org/10.1016/0022-1694\(91\)90048-M](https://doi.org/10.1016/0022-1694(91)90048-M), 1991.
- 797 Braun, L. N.: Simulation of snowmelt-runoff in lowland and lower alpine regions of Switzerland. Ph.D. thesis,
798 ETH Zurich, 1984.
- 799 Corripio, J.: Vectorial algebra algorithms for calculating terrain parameters from DEMs and solar radiation
800 modelling in mountainous terrain. *Int. J. Geogr. Inf. Sci.*, *Vol. 17*(1), pp. 1-23, <https://doi.org/10.1080/713811744>,
801 2003.
- 802 De Gregorio, L., Günther, D., Callegari, M., Strasser, U., Zebisch, M., Bruzzone, L. and Notarnicola, C.:
803 Improving SWE Estimation by Fusion of Snow Models with Topographic and Remotely Sensed Data. *Rem. Sens.*,
804 *11*(17), 2033, <https://doi.org/10.3390/rs11172033>, 2019a.
- 805 De Gregorio, L., Callegari, M., Marin, C., Zebisch, M., Bruzzone, L., Demir, B., Strasser, U., Marke, T., Günther,
806 D., Nadalet, R. and Notarnicola, C.: A novel data fusion technique for snow cover retrieval. *J. Sel. Top. Appl.*
807 *Earth Obs. Rem. Sens. JSTARS*, *Vol. 12*, No. 8, <https://doi.org/10.1109/JSTARS.2019.2920676>, 2019b.
- 808 Ebner, P. P., Koch, F., Premier, V., Marin, C., Hanzer, F., Carmagnola, C. M., Hugues, F., Günther, D., Monti, F.,
809 Hargoaa, O., Strasser, U., Morin, S. and Lehning, M.: Evaluating a prediction system for snow management. *The*
810 *Cryosphere*, <https://doi.org/10.5194/tc-15-3949-2021>, 2021.
- 811 Fischer, A., Seiser, B., Stocker-Waldhuber, M., Mitterer, C. and Abermann, J.: Tracing glacier changes in Austria
812 from the Little Ice Age to the present using a lidar-based high-resolution glacier inventory in Austria. *The*
813 *Cryosphere*, *9*(2), pp. 753–766, <https://doi.org/10.5194/tc-9-753-2015>, 2015.
- 814 Essery, R.: A factorial snowpack model (FSM 1.0). *Geosci. Model. Dev.* *8*, pp. 3867–3876,
815 <https://doi.org/10.5194/gmd-8-3867-2015>, 2015.
816
- 817 Essery, R., Rutter, N., Pomeroy, J., Baxter, R., Staehli, M., Gustafsson, D., Barr, A., Bartlett, P. and Elder, K.:
818 SNOWMIP2: An evaluation of forest snow process simulations. *Bull. Am. Met. Soc.*, *90* (8), pp. 1120–1136,
819 <https://doi.org/10.1175/2009BAMS2629.1>, 2009.
- 820 Essery, R., Morin, S., Lejeune, Y. and Ménard C. B.: A comparison of 1701 snow models using observations from
821 an alpine site. *Adv. Wat. Res.* *55*, pp.131–148, 2013.



- 822 Etchevers, P., Martin, E., Brown, R., Fierz, C., Lejeune, Y., Bazile, E., Boone, A., Dai, Y.-J., Essery, R. L. E.,
823 Fernandez, Y., Gusev, Y., Jordan, R., Foren, V., Kowalczyk, E., Nasonova, N. O., Pyles, R. D., Schlosser, A.,
824 Shmakin, A. B., Smirnova, T. G., Strasser, U., Verseghy, D., Yamazaki, T. and Yang, Z.-L.: Validation of the
825 surface energy budget simulated by several snow models (SnowMIP project). *Ann. Glaciol.*, Vol. 38, pp. 150–
826 158, <https://doi.org/10.3189/172756404781814825>, 2004.
- 827 Förster, K., Hanzer, F., Winter, B., Marke, T. and Strasser, U.: MELODIST – An open-source Meteorological
828 observation time series DISaggregation Tool. *Geosci. Model Dev.*, Vol. 9, pp. 2315–2333,
829 <https://doi.org/10.5194/gmd-9-2315-2016>, 2016.
- 830 Goodison, B. E., Louie, P., and Yang, D.: WMO solid precipitation measurement intercomparison. Tech. Rep.
831 WMO/TD 872, Geneva, 1998.
- 832 Gruber, S.: A mass-conserving fast algorithm to parameterize gravitational transport and deposition using digital
833 elevation models. *Water Resour. Res.*, Vol. 43, W06412, <https://doi.org/10.1029/2006WR004868>, 2007.
- 834 Grünewald, T., Bühler, Y. and Lehning, M.: Elevation dependency of mountain snow depth. *The Cryosphere*, 8,
835 pp. 2381–2394, <https://doi.org/10.5194/tc-8-2381-2014>, 2014.
- 836 Grünewald, T., Stötter, J., Pomeroy, J. W., Dadic, R., Moreno Baños, I., Marturià, J., Spross, M., Hopkinson, C.,
837 Burlando, P. and Lehning, M.: Statistical modelling of the snow depth distribution in open alpine terrain. *Hydrol.*
838 *Earth Syst. Sci.*, Vol. 17, pp. 3005–3021, <https://doi.org/10.5194/hess-17-3005-2013>, 2013.
- 839 Günther, D., Marke, T., Essery, R. and Strasser, U.: Uncertainties in Snowpack Simulations – Assessing the Impact
840 of Model Structure, Parameter and Forcing Data Error on Point-Scale Energy-Balance Snow Model Performance.
841 *Water Resour. Res.*, Vol. 55, pp. 2779–2800, <https://doi.org/10.1029/2018WR023403>, 2019.
- 842 Günther, D., Hanzer, F., Warscher, M., Essery, R. and Strasser, U.: Including parameter uncertainty in an
843 intercomparison of physically-based snow models. *Front. Earth Sci.*, Vol. 8, 542599,
844 <https://doi.org/10.3389/feart.2020.542599>, 2020.
- 845 Hanzer, F., Marke, T. and Strasser, U.: Distributed, explicit modelling of technical snow production for a ski area
846 in the Schladming Region (Austrian Alps). *Cold Reg. Sci. Technol.*, Vol. 108, pp. 113–124,
847 <https://doi.org/10.1016/j.coldregions.2014.08.003>, 2014.
- 848 Hanzer, F., Helfricht, K., Marke, T. and Strasser, U.: Multi-level spatiotemporal validation of snow/ice mass
849 balance and runoff modeling in glacierized catchments. *The Cryosphere*, Vol. 10, pp. 1859–1881,
850 <https://doi.org/10.5194/tc-10-1859-2016>, 2016.
- 851 Hanzer, F., Förster, K., Nemeč, J. and Strasser, U.: Projected hydrological and cryospheric impacts of 21st century
852 climate change in the Ötztal Alps (Austria) simulated using a physically based approach. *Hydrol. Earth Syst. Sci.*,
853 Vol. 22, 1593–1614, <https://dx.doi.org/10.5194/hess-22-1593-2018>, 2018.
- 854 Hanzer, F., Carmagnola, C. M., Ebner, P. P., Koch, F., Monti, F., Bavay, M., Bernhardt, M., Lafaysse, M.,
855 Lehning, M., Strasser, U., François, H. and Morin, S.: Simulation of snow management in Alpine ski resorts using
856 three different snow models. *Cold Reg. Sci. Technol.*, Vol. 172, 102995,
857 <https://doi.org/10.1016/j.coldregions.2020.102995>, 2020.
- 858 Hanzer, F., Warscher, M. and Strasser, U.: openAMUNDSEN v0.8.3 (v0.8.3). Zenodo.
859 <https://doi.org/10.5281/zenodo.10462109>, 2023.
- 860 Harris, C. R., Millman, K. J., van der Walt, S. J., Gommers, R., Virtanen, P., Cournapeau, D., Wieser, E., Taylor,
861 J., Berg, S., Smith, N. J., Kern, R., Picus, M., Hoyer, S., van Kerkwijk, M. H., Brett, M., Haldane, A., del Río, J.
862 F., Wiebe, M., Peterson, P., Gérard-Marchant, P., Sheppard, K., Reddy, T., Weckesser, W., Abbassi, H., Gohlke,
863 C and Oliphant, T. E.: Array programming with NumPy. *Nature*, 585(7825), 7825, <https://doi.org/10.1038/s41586-020-2649-2>, 2020.



- 865 Huss, M. and Farinotti, D.: Distributed ice thickness and volume of all glaciers around the globe. *J. Geophys. Res.*
866 *Earth Surface*, Vol. 117, F04010, <https://doi.org/10.1029/2012JF002523>, 2012.
- 867 Helfricht, K.: Analysis of the spatial and temporal variation of seasonal snow accumulation in Alpine catchments
868 using airborne laser scanning. Ph.D. thesis, Innsbruck, 2014.
- 869 Hoyer, S. and Hamman, J.: xarray: N-D labeled Arrays and Datasets in Python. *Journal Open Res. Soft.*, 5(1),
870 <https://doi.org/10.5334/jors.148>, 2017.
- 871 Kochendorfer, J., Rasmussen, R., Wolff, M., Baker, B., Hall, M. E., Meyers, T., Landolt, S., Jachcik, A., Isaksen,
872 K., Brækkan, R. and Leeper, R.: The quantification and correction of wind-induced precipitation measurement
873 errors. *Hydrol. Earth Syst. Sci.*, 21(4), pp. 1973–1989, <https://doi.org/10.5194/hess-21-1973-2017>, 2017.
- 874 Koivusalo, H., Heikinheimo, M. and Karvonen, T.: Test of a simple two-layer parameterisation to simulate the
875 energy balance and temperature of a snow pack. *Theor. Appl. Clim.*, 70(1–4), pp. 65–79,
876 <https://doi.org/10.1007/s007040170006>, 2001.
- 877 Kratzert, F., Gauch, M., Nearing, G., Hochreiter, S and Klotz, D.: Niederschlags-Abfluss-Modellierung mit Long
878 Short-Term Memory (LSTM). *Österr. Wasser- und Abfallw.*, <https://doi.org/10.1007/s00506-021-00767-z>, 2023.
- 879 Krinner, G., Derksen, C., Essery, R., Flanner, M., Hagemann, S., Clark, M., Hall, A., Rott, H., Brutel-Vuilmet,
880 C., Kim, H., Ménard, C., Mudryk, L., Thackeray, C., Arduini, G., Bartlett, P., Boone, A., Chéruey, F., Colin, J.,
881 Cuntz, M., Dai, Y., Decharme, B., Derry, J., Ducharme, A., Dutra, E., Fang, X., Fierz, C., Ghattas, J., Gusev, Y.,
882 Haverd, V., Kontu, A., Lafaysse, M., Law, R., Lawrence, D., Li, W., Marke, T., Marks, D., Nasonova, O., Nitta,
883 T., Niwano, M., Pomeroy, J., Raleigh, M. S., Schaedler, G., Semenov, V., Smirnova, T., Stacke, T., Strasser, U.,
884 Svenson, S., Turkov, D., Wang, L., Wang, T., Wever, N., Yuan, H. and Zhou, W.: ESM-SnowMIP: Assessing
885 models and quantifying snow-related climate feedbacks. *Geosci. Model Dev.*, 5027–5049,
886 <https://doi.org/10.5194/gmd-11-5027-2018>, 2018.
- 887 Lam, S. K., Pitrou, A. and Seibert, S.: Numba: A llvm-based python jit compiler. *Proceedings of the Second*
888 *Workshop on the LLVM Compiler Infrastructure in HPC*, pp. 1–6, 2015.
- 889 Lam, R., Sanchez-Gonzalez, A., Wilson, M., Wirmsberger, P., Fortunato, M., Alet, F., Ravuri, S., Ewalds, T.,
890 Eaton-Rosen, Z., Hu, W., Merose, A., Hoyer, S., Holland, G., Vinyals, O., Stott, J., Pritzel, A., Mohamed, S. and
891 Battaglia, P.: Learning skillfull medium-range global weather forecasting. *Science* 382, pp. 1416–1421,
892 <https://www.science.org/doi/10.1126/science.adi2336>, 2023.
- 893 Lehning, M., Bartelt, P., Brown, B., Russi, T., Stockli, U. and Zimmerli, M.: SNOWPACK model calculations for
894 avalanche warning based upon a new network of weather and snow stations. *Cold Reg. Sci. Technol.*, Vol. 30, pp.
895 145–157, 1999.
- 896 Lindström, G.: A Simple Automatic Calibration Routine for the HBV Model. *Nord. Hydrol.*, Vol. 28, pp. 153–
897 168, 1997.
- 898 Liston, G. E. and Elder, K.: A meteorological distribution system for high-resolution terrestrial modeling
899 (MicroMet). *J. Hydrometeor.*, 7(2), pp. 217–234, <https://doi.org/10.1175/JHM486.1>, 2006.
- 900 McKinney, W.: Data Structures for Statistical Computing in Python. *Proceedings of the 9th Python in Science*
901 *Conference*, pp. 56–61, <https://doi.org/10.25080/Majora-92bf1922-00a>, 2010.
- 902 Menard, C., Essery, R., Krinner, G., Arduini, G., Bartlett, P., Boone, A., Brutel-Vuilmet, C., Burke, E., Cuntz, M.,
903 Dai, Y., Decharme, B., Dutra, E., Fang, L., Fierz, C., Gusev, Y., Hagemann, S., Haverd, V., Kim, H., Lafaysse,
904 M., Marke, T., Nasonova, O., Nitta, T., Niwano, M., Pomeroy, J., Schaedler, G., Semenov, V., Smirnova, T.,
905 Strasser, U., Swenson, S., Turkov, D., Wever, N. and Yuan, H.: Scientific and human errors in a snow model
906 intercomparison. *Bull. Amer. Meteor. Soc.*, <https://doi.org/10.1175/BAMS-D-19-0329.1>, 2021.
- 907 Marke, T., Strasser, U., Hanzer, F., Wilcke, R., Gobiet, A. and Stötter, J.: Scenarios of future snow conditions in
908 Styria (Austrian Alps). *J. Hydrometeor.*, Vol. 16, pp. 261–277, <https://doi.org/10.1175/JHM-D-14-0035.1>, 2015.



- 909 Marke, T., Mair, E., Förster, K., Hanzer, F., Garvelmann, J., Pohl, S., Warscher, M. and Strasser, U.:
910 ESCIMO.spread (v2): Parameterization of a spreadsheet-based energy balance snow model for inside-canopy
911 conditions, *Geosci. Model Dev.*, Vol. 9, 633–646, <https://doi.org/10.5194/gmd-9-633-2016>, 2016.
- 912 Marke, T., Hanzer, F., Olefs, M. and Strasser, U.: Simulation of Past Changes in the Austrian Snow Cover 1948-
913 2009. *J. Hydrometeor.*, Vol. 19, pp. 1529–1545, <https://doi.org/10.1175/JHM-D-17-0245.1>, 2018.
- 914 Mauser, W., Prasch, M. and Strasser, U.: Physically based Modelling of Climate Change Impact on Snow Cover
915 Dynamics in Alpine Regions using a Stochastic Weather Generator. *Proceedings of the International Congress on
916 Modelling and Simulation MODSIM07 2007*, Christchurch, New Zealand, 2007.
- 917 Mott, R., Winstral, A., Cluzet, B., Helbig, N., Magnusson, J., Mazzotti, G., Quéno, L., Schirmer, M., Webster, C.
918 and Jonas, T.: Operational snow-hydrological modeling for Switzerland. *Front. Earth Sci.*, 11:1228158,
919 <https://doi.org/10.3389/feart.2023.1228158>, 2023.
- 920 Nash, J. E.: A unit hydrograph study, with particular reference to British catchments. *Proc. Inst. Civ. Eng.*, Vol.
921 17, pp. 249–282, 1960.
- 922 Ohmura, A.: Physical basis for the temperature-based melt-index method. *J. Appl. Meteor.*, Vol. 40, pp. 753–761,
923 2001.
- 924 Pellicciotti, F., Brock, B., Strasser, U., Burlando, P., Funk, M. and Corripio, J.: An enhanced temperature-index
925 glacier melt model including shortwave radiation balance: development and testing for Haut Glacier D’Arolla,
926 Switzerland. *J. Glaciol.*, Vol. 51, Nr. 175, pp. 573–587, <https://doi.org/10.3189/172756505781829124>, 2005.
- 927 Pfeiffer, J., Zieher, T., Schmieder, J., Rutzinger, M. and Strasser, U.: Spatio-temporal assessment of the
928 hydrological drivers of an active deep-seated gravitational slope deformation – the Vögelsberg landslide in Tyrol
929 (Austria). *Earth Surf. Proc. Landf.*, <http://doi.org/10.1002/esp.5129>, 2021.
- 930 Podsiadło, I., Paris, C., Callegari, M., Marin, C., Günther, D., Strasser, U., Notarnicola, C. and Bruzzone, L.:
931 Integrating models and remote sensing data for distributed glacier mass balance estimation. *J. Sel. Top. Appl.
932 Earth Obs. Rem. Sens. JSTARS*, Vol. 13, pp. 6177–6194, <https://doi.org/10.1109/JSTARS.2020.3028653>, 2020.
- 933 Quéno, L., Mott, R., Morin, P., Cluzet, B., Mazzotti, G. and Jonas, T.: Snow redistribution in an intermediate-
934 complexity snow hydrology modelling framework. *EGUsphere [preprint]*, <https://doi.org/10.5194/egusphere-2023-2071>, 2023.
- 936 Rasmussen, R., Baker, B., Kochendorfer, J., Meyers, T., Landolt, S., Fischer, A. P., Black, J., Thériault, J. M.,
937 Kucera, P., Gochis, D., Smith, C., Nitu, R., Hall, M., Ikeda, K. and Gutman, E.: How well are we measuring snow?
938 The NOAA/FAA/NCAR Winter Precipitation Test Bed. *Bull. Am. Met. Soc.*, pp. 811–829.
939 <https://doi.org/10.1175/BAMS-D-11-00052.1>, 2012.
- 940 Rohrer, M. B.: Die Schneedecke im schweizerischen Alpenraum und ihre Modellierung. *Zürcher Geographische
941 Schriften*, 49, 178, 1992.
- 942 Rutter, N., Essery, R. L. E., Pomeroy, J., Altimir, N., Andreadis, K., Baker, I., Barr, A., Bartlett, P., Elder, K.,
943 Ellis, C., Feng, X., Gelfan, A., Goodbody, G., Gusev, Y., Gustafsson, D., Hellström, R., Hirota, T., Jonas, T.,
944 Koren, V., Li, W.-P., Luce, C., Martin, E., Nasonova, O., Pumpanen, J., Pyles, D., Samuelsson, P., Sandells, M.,
945 Schädler, G., Shmakin, A., Smirnova, T., Stähli, M., Stöckli, R., Strasser, U., Su, H., Suzuki, K., Takata, K.,
946 Tanaka, K., Thompson, E., Vesala, T., Viterbo, P., Wiltshire, A., Xue, Y. and Yamazaki, T.: Evaluation of forest
947 snow processes models (SnowMIP2). *J. Geophys. Res.*, 114, D06111, <https://doi.org/10.1029/2008JD011063>,
948 2009.
- 949 Sauter, T., Arndt, A. and Schneider, C.: COSIPY v1.3 – an open-source coupled snowpack and ice surface energy
950 and mass balance model. *Geosci. Model Dev.*, Vol. 13, pp. 5645–5662, <https://doi.org/10.5194/gmd-13-5645-2020>,
951 2020.



- 952 Seibert, J. and Bergström, S.: A retrospective on hydrological catchment modelling based on half a century with
953 the HBV model. *Hydrol. Earth Syst. Sci.*, Vol. 26, pp. 1371–1388, <https://doi.org/10.5194/hess-26-1371-2022>,
954 2022.
- 955 Seidl, R., Rammer, W., Scheller, R. M. and Spies, T. A.: An individual-based process model to simulate landscape-
956 scale forest ecosystem dynamics. *Ecol. Mod.*, Vol. 231, <https://doi.org/10.1016/j.ecolmodel.2012.02.015>, 2012.
- 957 Sicart, J. M., Ramseyer, V., Picard, G., Arnaud, L., Coulaud, K., Freche, G., Soubeyrand, D., Lejeune, Y., Dumont,
958 M., Gouttevin, I., Le Gac, E., Berger, F., Monnet, J.-M., Borgniet, L., Mermin, E., Rutter, N., Webster, C. and
959 Essery, N.: Snow accumulation and ablation measurements in a midlatitude mountain coniferous forest (Col de
960 Porte, France, 1325 m altitude): the Snow Under Forest (SnoUF) field campaign data set. *Earth Syst. Sci. Data*,
961 Vol. 15, <https://doi.org/10.5194/essd-15-5121>, 2023.
- 962 Strasser, U. and Mauser, W.: Modelling the Spatial and Temporal Variations of the Water Balance for the Weser
963 Catchment 1965-1994. *J. Hydrol.*, Vol. 254/1-4, pp. 199–214, [https://doi.org/10.1016/S0022-1694\(01\)00492-9](https://doi.org/10.1016/S0022-1694(01)00492-9),
964 2001.
- 965 Strasser, U., Etchevers, P. and Lejeune, Y.: Intercomparison of two Snow Models with Different Complexity
966 Using Data from an Alpine Site. *Nordic Hydrol.*, 33 (1), pp. 15–26, <https://doi.org/10.2166/nh.2002.0002>, 2002.
- 967 Strasser, U., Corripio, J., Brock, B., Pellicciotti, F., Burlando, P. and Funk, M. (2004): Spatial and Temporal
968 Variability of Meteorological Variables at Haut Glacier d’Arolla (Switzerland) During the Ablation Season 2001:
969 Measurements and Simulations. *J. Geophys. Res.*, Vol. 109, D03103, <https://doi.org/10.1029/2003JD003973>,
970 2004.
- 971 Strasser, U.: Die Modellierung der Gebirgsschneedecke im Nationalpark Berchtesgaden. Modelling of the
972 mountain snow cover in the Berchtesgaden National Park. Berchtesgaden National Park research report, Nr. 55,
973 ISBN 978-3-922325-62-8, Berchtesgaden, 2008.
- 974 Strasser, U., Bernhardt, M., Weber, M., Liston, G. E. and Mauser, W.: Is snow sublimation important in the alpine
975 water balance? *The Cryosphere*, Vol. 2, pp. 53–66, <https://doi.org/10.5194/tc-2-53-2008>, 2008.
- 976 Strasser, U. and Marke, T.: ESCIMO.spread - a spreadsheet-based point snow surface energy balance model to
977 calculate hourly snow water equivalent and melt rates for historical and changing climate conditions. *Geosci.*
978 *Model Dev.*, Vol. 3, pp. 643–652, <https://doi.org/10.5194/gmd-3-643-2010>, 2010.
- 979 Strasser, U., Warscher, M. and Liston, G. E.: Modelling snow-canopy processes on an idealized mountain. *J.*
980 *Hydrometeor.* Vol. 12, No. 4, pp. 663–677, <https://doi.org/10.1175/2011JHM1344.1>, 2011.
- 981 Strasser, U., Marke, T., Braun, L., Escher-Vetter, H., Juen, I., Kuhn, M., Maussion, F., Mayer, C., Nicholson, L.,
982 Niederscheider, K., Sailer, R., Stötter, J., Weber, M. and Kaser, G.: The Rofental: a high Alpine research basin
983 (1890–3770 m a.s.l.) in the Ötztal Alps (Austria) with over 150 years of hydrometeorological and glaciological
984 observations. *Earth Syst. Sci. Data*, Vol. 10, pp. 151–171, <https://doi.org/10.5194/essd-10-151-2018>, 2018. Data
985 available at <https://doi.org/10.1594/PANGAEA.876120>.
- 986 Vionnet, V., Brun, E., Morin, S., Boone, A., Faroux, S., Le Moigne, P., Martin, E. and Willemet, J.-M.: The
987 detailed snowpack scheme Crocus and its implementation in SURFEX v7.2. *Geosci. Model Dev.*, Vol. 5, pp. 773–
988 791, <https://doi.org/10.5194/gmd-5-773-2012>, 2012.
- 989 Vionnet, V., Marsh, C. B., Menounos, B., Gascoïn, S., Wayand, N., Shea, J., Mukherjee, K. and Pomeroy, J.:
990 Multi-scale snowdrift-permitting modelling of mountain snowpack. *The Cryosphere*, Vol. 15, pp. 743–769,
991 <https://doi.org/10.5194/tc-15-743-2021>, 2021.
- 992 Vionnet, V., Verville, M., Fortin, V., Brugman, M., Abrahamowicz, M., Lemay, F., Thériault, M., Lafaysse, T.
993 and Milbrandt, J.-A.: Snow level from post-processing of atmospheric model improves snowfall estimate and
994 snowpack prediction in mountains. *Water Resour. Res.*, Vol. 58, e2021WR031778,
995 <https://doi.org/10.1029/2021WR031778>, 2022.



- 996 Viviroli, D., Dürr, H. H., Messerli, B., Meybeck, M. and Weingartner, R.: Mountains of the world, water towers
997 for humanity: Typology, mapping, and global significance. *Water Resour. Res.*, 43 (7),
998 <https://doi.org/10.1029/2006wr005653>, 2007.
- 999 Viviroli, D., Kumm, M., Meybeck, M., Kallio, M. and Wada, Y.: Increasing dependence of lowland populations
1000 on mountain water resources. *Nature Sustainability*, Nature Publishing Group, 3(11), pp. 917–928,
1001 <https://doi.org/10.1038/s41893-020-0559-9>, 2020.
- 1002 Warscher, M., Strasser, U., Kraller, G., Marke, T., Franz, H. and Kunstmann, H.: Performance of complex snow
1003 cover descriptions in a distributed hydrological model system: A case study for the high Alpine terrain of the
1004 Berchtesgaden Alps. *Water Resour. Res.*, Vol. 49, pp. 2619–2637, <https://doi.org/10.1002/wrcr.20219>, 2013.
- 1005 Warscher, M., Marke, T., Rottler, E. and Strasser, U.: Operational and experimental snow observation systems in
1006 the upper Rofental: data from 2017–2023. *EGUsphere* [preprint], <https://doi.org/10.5194/essd-2024-45>,
1007 2024.
- 1008 Weber, M.: A parameterization for the turbulent fluxes over melting surfaces derived from eddy correlation
1009 measurements. In: Strasser, U. and Vogel M. (eds.) (2008): *Proceedings of the Alpine*Snow*Workshop*, Munich,
1010 October 5–6, 2006, Germany. Berchtesgaden National Park research report 53, ISBN13 978-3-922325-60-4,
1011 Berchtesgaden, 2008.
- 1012 Yokoyama, R., Shirasawa, M. and Pike, R. J.: Visualizing topography by openness: a new application of image
1013 processing to digital elevation models. *Photogr. Eng. Rem. Sens.*, Vol. 68, pp. 257–266, 2002.